Earth-Science Reviews 226 (2022) 103930

Contents lists available at ScienceDirect

Earth-Science Reviews

journal homepage: www.elsevier.com/locate/earscirev

Temporal changes in subduction- to collision-related magmatism in the Neotethyan orogen: The Southeast Iran example

Hadi Shafaii Moghadam [a,b,c,d,*], Qiu-Li Li [b,**], William L. Griffin [d], Robert J. Stern [e], Jose F. Santos [f], Mihai N. Ducea [g,h], Chris J. Ottley [i], Orhan Karsli [j], Fatemeh Sepidbar [a], Suzanne Y. O'Reilly [d]

[a] School of Earth Sciences, Damghan University, Damghan 36716-41167, Iran
[b] Institute of Geology and Geophysics, Chinese Academy of Sciences, Beijing 100029, China
[c] FB4-Dynamics of the Ocean Floor, GEOMAR, Helmholtz-Zentrum für Ozeanforschung Kiel, Wischhofstr. 1-3, D-24148 Kiel, Germany
[d] CCFS and GEMOC ARC National Key Centre, Macquarie University, NSW 2109, Australia
[e] Geosciences Dept. University of Texas at Dallas, Richardson, TX 75083-0688, USA
[f] Geobiotec, Universidade de Aveiro, 3810-193 Aveiro, Portugal
[g] University of Arizona, Tucson, AZ 85721, USA
[h] Faculty of Geology and Geophysics, University of Bucharest, 010041, Bucharest, Romania
[i] Department of Earth Sciences, University of Durham, Durham, DH1 3LE, UK
[j] Department of Geological Engineering, Karadeniz Technical University, Trabzon TR-61080, Turkey

ARTICLE INFO

Keywords:
Continental arc
Continental collision
Adakite
Urumieh-Dokhtar Magmatic Belt
Iran

ABSTRACT

Continental-arc igneous rock compositions change in response to the transition from subduction to collision and these changes can reveal how the crust, lithosphere and magma sources evolved. Neotethys-related Late Cretaceous to Pleistocene subduction- and collision-related magmatic rocks from the ~350 km long southeast Urumieh-Dokhtar Magmatic Belt (UDMB) of Iran provide an excellent natural laboratory to better understand these changes. These igneous rocks are well-exposed and moderately eroded to reveal a nearly complete record since subduction initiation at ~95 Ma. We analyzed new samples for major and trace elements (83 samples), Sr—Nd isotopic compositions (47 samples), and U—Pb zircon ages (26 samples) and compiled geochemical and geochronological data on the southeast segment of the UDMB. The geochronological data reveal two magmatic pulses at ~80–70 Ma and ~50–0 Ma. Important changes in magmatic compositions reflect initial collision with Arabia at ~32 Ma, changing from normal calc-alkaline to increasingly adakitic immediately after collision began. Five stages can be identified: 1) normal continental-arc magmatism during the Late Cretaceous; 2) arc quiescence in Paleocene and Early Eocene time; 3) Middle-Late Eocene extensional arc magmatism related to slab rollback; 4) early collision and crustal thickening during the Early Oligocene; and 5) slab breakoff, asthenospheric upwelling, and associated adakitic magmatism from Middle Miocene onward. Temporal changes in UDMB magmas reflect the response of the overriding plate to changes in the geometry of the subducting Neotethyan lithosphere and to collision between Arabia and Iran. Crustal thickening and arc narrowing during Miocene to Pleistocene post-collisional magmatism caused adakitic magmatism and associated Cu mineralization. Zircon O—Hf and apatite O isotopes as well as bulk-rock Nd isotopes of Cu-bearing adakitic rocks are similar to other barren rocks, but nearly all fertile rocks have higher Hf/Y, $Eu/Eu^*_{(n)}$ in zircon and higher Sr/Y, V/Y, $Eu/Eu^*_{(n)}$ in apatite than barren rocks.

1. Introduction

Magmatic arcs form on the upper plate of convergent plate margins; these margins change tectonic conditions due to buoyancy changes in the down-going plate. These induce changes in magma production and sources that are reflected in the geochemical and isotopic signatures of

* Corresponding author at: School of Earth Sciences, Damghan University, Damghan 36716-41167, Iran.
** Corresponding author at: Institute of Geology and Geophysics, Chinese Academy of Sciences, Beijing 100029, China.
E-mail addresses: hadishafaii@du.ac.ir (H.S. Moghadam), liqiuli@mail.iggcas.ac.cn (Q.-L. Li).

https://doi.org/10.1016/j.earscirev.2022.103930
Received 24 June 2021; Received in revised form 30 December 2021; Accepted 14 January 2022
Available online 19 January 2022

igneous rocks (DeCelles et al., 2009; Ducea et al., 2015). Arc magmatism associated with normal subduction is well documented and is characterized by arc-like magmas depleted in Nb—Ta and enriched in large ion lithophile elements such as Rb, Ba, Th, U, K, Pb and La. Convergent margins continue to deliver arc-like magmas even during and for some time after continental collision as continental lithosphere begins to subduct. In several places, very young or ongoing magmatic activity occurs in collision zone that is not related to oceanic subduction, such as the Carpathians or the Caucasus (e.g., Bindeman et al., 2021; Seghedi and Downes, 2011). Collision-related magmatic products have similar bulk chemistry (in both major-trace elements and isotopes) to subduction magmatism, and are dominated by calc-alkaline andesites, dacites and rhyolites as well as their plutonic equivalents. However, several workers suggest that *syn*-collisional magmatism is more alkali-rich and/or adakitic, and those features (among others) illuminate different melting regimes and igneous processes in subduction versus collision settings. Although numerous papers have addressed this issue, the textbook view on collision-related magmatism continues to centre on leucogranites and S-type granites formed by partial melting of continental crust and metasediments thickened in continental collision zones (e.g., Nabelek, 2020). This view needs to be modified to encompass other products found in modern collision belts. The Tethys orogen of southern Eurasia – where all Cenozoic continental collisions happened – is the best place to study examples of collisional magmatism (e.g., Chiu et al., 2013; Sepidbar et al., 2019; Verdel et al., 2011).

Addressing this problem benefits from investigating transitions from subduction to collision in the geologic record to see how magmatism changed over geologically short time scales. The problem with this approach in most places along the Tethys orogen is that the timing of the suturing is often not well enough constrained. For example, in the Himalaya-Tibet region, uncertainties linger as to exactly when collision started (Zhang et al., 2012), and while volcanic rocks spanning the transition may exist (e.g., the Linzizong volcanic rocks in southern Tibet; Liu et al., 2018); end-member models for collision initiation diverge by tens of million years. Similar uncertainties plague studies of Carpathian igneous rocks, where some envision that an oceanic slab was present until recently (Matenco et al., 2010), while others argue that continental collision was the sole driver of young magmatism (Ducea et al., 2020).

This paper reports on the results of multiple analytical approaches to understand the temporal evolution of magmatism in the southeast Urumieh-Dokhtar Magmatic Belt (UDMB) of Iran and shows how this changed from subduction to collision. Our results are interpreted to help us understand the geochemical changes during this important transition and the relations between collision-related magmatism and porphyry Cu mineralization.

2. Background geology

The Cenozoic magmatic arc of Iran is well-suited for understanding the temporal evolution of convergent margin magmatism, because we know when subduction initiation occurred (at ~95 Ma, Stern et al., 2021), it contains numerous volcanic and intrusive products from the Late Cretaceous to the Pleistocene and the beginning of collision in the Oligocene is well resolved in the geologic record (e.g., McQuarrie and van Hinsbergen, 2013). This broad magmatic arc preserves ~80 Myr of magmatism over an area up to 1000 km wide from east to west and north to south (Fig. 1A), recording the subduction of Neotethys oceanic lithosphere beneath Iran. Continental collision between Arabia and Eurasia occurred at *ca* 27 Ma (McQuarrie and van Hinsbergen, 2013), although some argue that the "soft" collision (characterized by lower rate of deformation, uplift, and exhumation of the Iranian plateau during earliest stage of collision) started at ~32 Ma (Early Oligocene) (e.g., Allen and Armstrong, 2008; Mouthereau et al., 2012; Tadayon et al., 2017). It is also suggested that the "soft" collision was followed by "hard" collision beginning ~20 Ma, characterized by shortening and thickening of Iranian continental crust, causing more deformation, uplift, and exhumation (e.g., Madanipour et al., 2017; Madanipour et al., 2013). Extensive crustal thickening occurred during increased shortening at ~20 Ma (Ballato et al., 2013), which is consistent with recent geochemical evidence from the Urumieh-Dokhtar Magmatic Belt (UDMB), which indicates that crustal thickening to ~60–50 km culminated during the Early-Middle Miocene (Chaharlang et al., 2020).

The UDMB, which marks the magmatic front of the broad magmatic arc in Iran, is 40–70 km wide and trends northwest-southeast for ~1000 km across Iran. UDMB arc magmatism began with subduction in the Late Cretaceous, matured in the Paleogene and waned after collision with Arabia in the Neogene (e.g., Babazadeh et al., 2017; Hosseini et al., 2017; Moghadam et al., 2020; Yeganehfar et al., 2013). Moderate erosion of the UDMB has exposed both its volcanic and shallow plutonic levels, especially in the southeast portion of UDMB (Chaharlang et al., 2020; Sepidbar et al., 2019). The Cenozoic igneous rocks of Iran and their extension to the northwest of the Neotethyan orogenic belt (Caucasus region of Georgia-Armenia-Azerbaijan and the eastern Pontides of Turkey) and east (Afghanistan, Pakistan and Tibet) also host abundant Cenozoic precious- and base-metal epithermal and porphyry Cu deposits (Moritz et al., 2016).

In addition to the magmatic front (the UDMB), there are magmatic belts in the north-northwest, northeast, and eastern parts of Iran that define the magmatic back-arc regions. The Alborz-Azerbaijan belt (north-northwest Iran, Fig. 1A), continues into the magmatic belts of the Lesser Caucasus and Pontides (Turkey) (Castro et al., 2013). It is constructed on Upper Jurassic-Late Cretaceous flysch and platform carbonates, and mostly consists of Eocene volcanic rocks intruded by shoshonitic Oligocene-Miocene intrusive rocks (Jamali et al., 2010). An ensialic back-arc basin setting is suggested for the formation of the Alborz-Azerbaijan magmatic rocks (Asiabanha and Foden, 2012). This belt hosts significant Cenozoic epithermal deposits in Iran (Siani et al., 2020), although Cu porphyry-type ore deposits are also common. These Cu porphyry deposits have molybdenite *Re*—Os ages of 28.2 ± 0.4 to 20.5 ± 3.6 Ma and zircon U—Pb data ages of 21.1 ± 0.2 to 19.3 ± 0.3 Ma (Aghazadeh et al., 2015).

The Birjand-Zahedan back-arc magmatic belt (eastern Iran, Fig. 1A) includes a thick sequence of Late Cretaceous-Paleocene volcano-sedimentary rocks, which are covered by Eocene-Oligocene (^{40}Ar-^{39}Ar; 46–25 Ma) calc-alkaline to shoshonitic magmatic rocks. It has been proposed that the Paleogene magmatism in the Birjand-Zahedan magmatic belt was triggered by convective removal of lithosphere (delamination) and resultant asthenospheric upwelling accompanying extensional collapse (Pang et al., 2012). Continued asthenospheric upwelling led to Late Miocene alkali basaltic volcanism (^{40}Ar-^{39}Ar; 14–11 Ma) (Pang et al., 2012). This belt also hosts minor Cu porphyry-type deposits with zircon U—Pb ages of 39.0 ± 0.8 and 37.3 ± 0.3 Ma (Aghazadeh et al., 2015).

The Sabzevar-Torud back-arc magmatic belt (northeast Iran) consists of a huge pile of Late Cretaceous to Miocene arc-related magmatic rocks, including calc-alkaline to adakitic plutons and abundant Late Cretaceous to Eocene rhyolite sheets and domes. Minor Cu porphyry deposits with hornblende and biotite ^{40}Ar—^{39}Ar ages of 42.7 ± 0.2 and 43.7 ± 0.1 Ma (from their potassic alteration zones) are common in this belt (Moghadam et al., 2020).

The southeast segment of the UDMB records both subduction- (80–27 Ma) and collision-related (27–0 Ma) magmatism and preserves temporal and along-arc variations in this evolution. Reconstructing magma genesis and magmatic evolution in the southeastern UDMB over the past 80 Ma can help us understand temporal geochemical variations in convergent margin magmas, since both earlier subduction-related and younger collision-related igneous rocks are abundant and well exposed in this desert region. Most giant Cu deposits of Iran are also found along the magmatic front of the southeastern UDMB (Fig. 1B). Mineralization in the southeastern UDMB occurred over an interval of about 20 m.y., for which two metallogenic epochs have been recognized (Aghazadeh et al., 2015): minor mineralization in Late Oligocene (~27 Ma) and

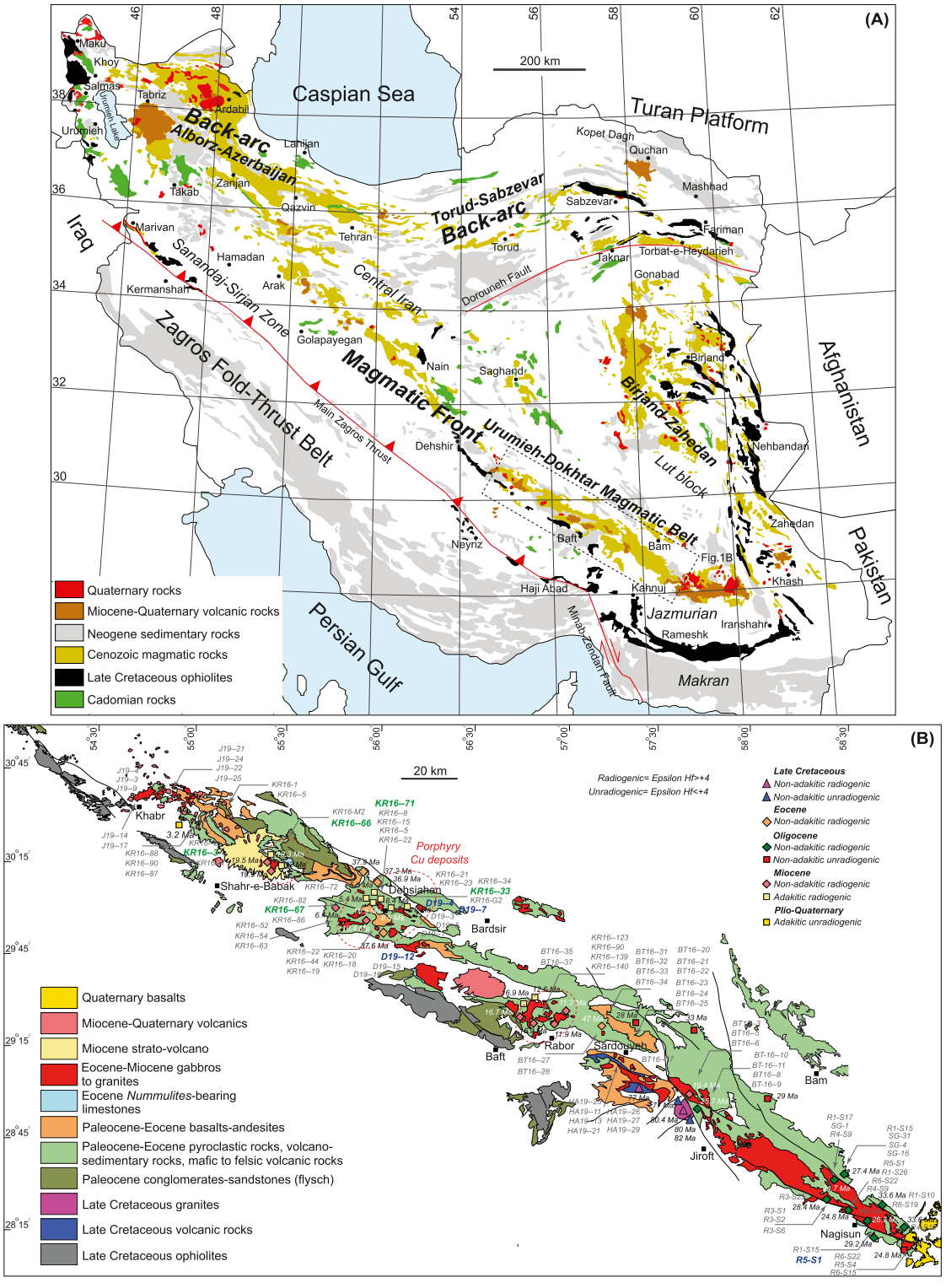

Fig. 1. A- Simplified geological map of Iran emphasizing Mesozoic ophiolites, Cenozoic magmatic rocks, Neogene sedimentary rocks and Miocene-Quaternary volcanic rocks. B- Geological map of the southeast segment of the UDMB, showing the distribution of Mesozoic-Cenozoic magmatic rocks. New and compiled zircon U—Pb data on magmatic rocks are shown. Compiled zircon U—Pb ages are from Asadi (2018) and Chiu et al. (2017). Dashed red circles show the location of the main porphyry Cu deposits. Dated samples are subdivided into radiogenic (zircon $\varepsilon Hf_{(t)} > +4$) and unradiogenic ($\varepsilon Hf_{(t)} < +4$) rocks. Coloured bold, *italic* numbers show location of samples selected for apatite analysis; blue-coloured are barren rocks while green-coloured are fertile rocks. (For interpretation of the references to colour in this figure legend, the reader is referred to the web version of this article.)

giant Cu mineralization in Miocene (~20–6 Ma).

3. The Southeastern Urumieh-Dokhtar magmatic belt

The southeast segment of the UDMB is ~350 km long and ~ 50 km wide (Fig. 1B). The post-subduction initiation magmatic succession includes minor outcrops of Late Cretaceous igneous rocks with zircon U—Pb ages of *ca* 82–77 Ma (Chiu et al., 2013; Hosseini et al., 2017). These are covered by Paleogene pyroclastic and volcano-sedimentary rocks and intruded by Middle Eocene-Early Oligocene unmineralized and Middle-Late Miocene Cu-bearing (fertile) plutons (Asadi, 2018; Raeisi et al., 2021; Shafiei et al., 2009; Wan et al., 2018). Fertile intrusions are mostly felsic and porphyritic subvolcanic stocks, whereas barren bodies are mostly holocrystalline gabbro to granite. Radiometric ages and stratigraphic data indicate that Paleocene-Early Eocene time witnessed minor eruptions of lavas and pyroclastic rocks, crosscut by rare Eocene lamprophyre dikes (Shafiei et al., 2009). Magmatic activity intensified during Middle to Late Eocene with calc-alkaline to shoshonitic basaltic to trachytic volcanism and intrusion of unmineralized (barren) plutonic rocks with strong arc-like geochemical signatures (Salehi Nejad et al., 2020). Eocene magmatism was followed by Early Oligocene calc-alkaline igneous pulses. Collision began at *ca* 32 Ma and magmatism may have stopped during a Middle Oligocene and Early Miocene magmatic lull (Verdel et al., 2011). Eocene-Oligocene volcaniclastics and intrusive rocks were uplifted, eroded and unconformably covered by Late Oligocene-Miocene red-beds and shallow-water limestones. Magmatism resumed in Middle Miocene time, with intrusions of Cu-bearing porphyritic subvolcanic stocks with adakitic signatures (Asadi et al., 2014); this change in the melting regime likely reflects crustal thickening accompanying collision (Chaharlang et al., 2020). Melting of hydrous garnet amphibolites and/or eclogites in the lower crust may have produced Miocene adakitic rocks (Kheirkhah et al., 2020; Wan et al., 2018). Slab breakoff and melting as Arabia and Eurasia continued to collide may have facilitated Miocene adakite formation (Omrani et al., 2008). Slab breakoff would allow asthenospheric upwelling, which is consistent with geophysical data for the region (Motaghi et al., 2015). Magmatism continued from Late Miocene to Pleistocene, with eruption of volcanic rocks including high Sr/Y dacites, high-K basalts to trachytes and olivine alkaline basalts along with growth of a few stratovolcanoes (Fig. 1B).

4. Analytical procedures

The analytical procedures include: 1) X-Ray Fluorescence (XRF) and Inductively Coupled Plasma-Mass Spectrometry (ICP-MS) for bulk-rock major- and trace-element analyses; 2) Cathodoluminescence (CL) imaging of zircons by Scanning Electron Microscope (SEM); 3) Laser Ablation Inductively Coupled Plasma-Mass Spectrometry (LA-ICPMS) for U—Pb zircon dating and in situ zircon and apatite trace-element analysis; 5) Secondary Ion Mass Spectrometry (SIMS) for U—Pb zircon dating and O isotopes; 6) Multi-Collector Inductively Coupled Plasma-Mass Spectrometry (MC- ICPMS) for zircon Lu—Hf and in situ Sr—Nd isotopic analysis of apatite; and 7) Thermal ionization mass spectrometry (TIMS) for Sr and Nd isotopes in bulk-rock samples. We sampled both plutonic and volcanic rocks from different southeastern UDMB locations to cover all rock units across the studied area; locations are shown in Fig. 1B. We also compiled data from published literatures. All analytical procedures, instrumentation, errors and other details are presented in “Appendix A".

5. Results

5.1. Samples

Our samples from southeastern UDMB (Fig. 1B) are subdivided into five groups according to age: Late Cretaceous (7 samples), Eocene (27 samples), Oligocene (39 samples), Miocene (26 samples), and Pliocene-Pleistocene (3 samples). We also compiled data on the southeastern UDMB from the literature (see Tables S1 to S6). Field relationships have also been used to constrain relative ages of undated lavas and dikes based on their relationship to dated volcanic and plutonic rocks. Brief petrographic descriptions of magmatic rocks from these five groups are presented below.

5.1.1. Late Cretaceous

Late Cretaceous samples include volcanic and plutonic rocks. Volcanic rocks are porphyritic basalts and andesites. Phenocrysts in basalts are mainly clinopyroxene, plagioclase and hornblende, with traces of iddingsitized olivine- in a glassy to intersertal groundmass. Plutonic rocks are gabbro to granodiorite and granite. Gabbros are dominated by plagioclase, hornblende and clinopyroxene (plagioclase >clinopyroxene >hornblende) whereas granodiorites and granites have plagioclase, hornblende, biotite, potash (K-) feldspar and quartz as the main rock-forming minerals. K-feldspar in granites include microcline and orthoclase as well as perthite intergrowths.

5.1.2. Eocene

Eocene samples include volcanic and plutonic rocks as well as lamprophyre dikes. Volcanic rocks comprise basalts, andesites and rhyolites which are mostly porphyritic. Basalts contain olivine, clinopyroxene, spinel and plagioclase in a microlitic to holohyaline groundmass. Andesites have plagioclase and amphibole phenocrysts and less clinopyroxene (<5–8 vol%) than basalts. Andesite groundmass is microlitic to holocrystalline with plagioclase phenocrysts. Rhyolites have sanidine and quartz phenocrysts in a devitrified groundmass with cryptocrystalline felsic minerals. Plutonic rocks comprise gabbros, diorites, tonalites and granodiorites-granites. Gabbros and diorites contain plagioclase, amphibole and clinopyroxene (25–30% clinopyroxene and 5–10% amphibole in gabbros; 10–15% clinopyroxene and 30–40% amphibole in diorites) whereas granodiorites and tonalites have plagioclase, amphibole, quartz with minor K-feldspar. Granites have K-feldspar (microcline, orthoclase and perthite), quartz, and biotite with minor amphibole and plagioclase (oligoclase-andesine). Lamprophyres contain clinopyroxene and amphibole phenocrysts in a holocrystalline groundmass.

5.1.3. Oligocene

Oligocene samples include both volcanic and plutonic rocks. Volcanic rocks range from basalt-andesite to dacite-rhyolite and trachyte, whereas plutonic rocks are diorite, tonalite, granodiorite and granite. Diorite and tonalites contain plagioclase, amphibole, alkali feldspar and quartz with minor clinopyroxene. Plagioclase and amphibole are common in tonalites and granodiorite while clinopyroxene is present in diorites. Quartz and alkali feldspar (±biotite) are the major components of tonalite and granite. Andesites and basalts contain plagioclase, clinopyroxene and amphibole in a microlitic to glassy groundmass. Amphibole is absent in basalts and these rocks contain olivine pseudomorphs. Dacites and rhyolites contain rare sanidine and plagioclase phenocrysts in a groundmass with felsic, cryptocrystalline texture. Fine-grained sanidine and sodic plagioclase show shape-preferred orientation (trachytic texture) in trachytes.

5.1.4. Miocene

Miocene plutonic rocks are mostly shallow porphyritic intrusions and some host Cu mineralization. Plutonic rocks change from gabbro to granite, but granodiorites and diorites (quartz diorites) are especially abundant. Diorites and granodiorites have clinopyroxene (<10%), amphibole, plagioclase, biotite, K-feldspar and quartz. Quartz diorites have 5–10% quartz, K-feldspar and biotite in addition to clinopyroxene, amphibole and plagioclase. Granodiorites, diorites and quartz diorites-as shallow intrusions- have large crystals of plagioclase in a fine-grained crystalline groundmass. Gabbros mostly contain clinopyroxene and

plagioclase with green amphibole (actinolite) overgrowth around some clinopyroxenes. Volcanic rocks comprise basalts and andesites to dacites. Basalts and andesites contain clinopyroxene, amphibole and plagioclase phenocrysts in a microlitic groundmass whereas dacites have plagioclase, amphibole, biotite and quartz phenocrysts in a devitrified groundmass.

5.1.5. Pliocene-Pleistocene

Pliocene-Pleistocene samples are volcanic rocks, changing from andesite to dacite-rhyolite. Dacites and rhyolites are weakly porphyritic with phenocrysts of plagioclase, sanidine and resorbed quartz in a glassy to microlitic texture. Andesites are mostly porphyritic with large crystals (~2–3 cm) of plagioclase and amphibole in an intersertal to microlitic groundmass.

5.2. Zircon U—Pb geochronology

We dated samples from the southeastern UDMB using both LA-ICPMS and SIMS analyses of zircons. Results are shown on Terra-Wasserburg plots in Figs. 2, 3 and Fig. S1 and are summarized in Tables S3 and S4. We also compiled data from the literature (see Tables S3 and S4). Our dated and compiled samples can be subdivided into five groups according to age: Late Cretaceous, Eocene, Oligocene, Miocene, and Pliocene-Pleistocene. Further details are presented below.

5.2.1. Late Cretaceous

Late Cretaceous samples are from the southeast parts of the study area (Fig. 1B). One granitic sample (HA16–10) analyzed during this study shows an age of 80.4 ± 0.5 Ma (Fig. 2). Compiled zircon U—Pb ages reported here also yield ages of 77.5 ± 0.8 Ma (granite), 79.5 ± 0.3 Ma (diorite), 80.8 ± 1.5 Ma (diorite), 81.8 ± 2.4 Ma (diorite), 78.1 ± 0.9 Ma (andesite) and 82.7 ± 2.8 Ma (andesite) (Hosseini et al., 2017). These results indicate that Late Cretaceous igneous activity began by *ca* 83 Ma and continued until at least 77 Ma.

5.2.2. Eocene

Our five Eocene samples include both volcanic and plutonic rocks. Plutonic rocks have zircon U—Pb ages of 47.03 ± 0.7 Ma (BT16–24, diorite) and 37.6 ± 0.3 Ma (D19–12, diorite). Volcanic rocks yield ages of 37.2 ± 0.5 Ma (KR16–22, rhyolite), 36.9 ± 0.4 Ma (KR16–5, rhyolite) and 37.9 ± 0.6 Ma (KR16–1, rhyolite). These results indicate that southeastern UDMB Eocene magmatism began by 47 Ma and continued until at least 37 Ma (Early Middle to Late Eocene).

5.2.3. Oligocene

Plutonic rocks have zircon U—Pb ages of 24.7 ± 1.0 Ma (R4-S9, granodiorite), 24.8 ± 1.2 Ma (R6-S22, granite), 28.4 ± 0.9 Ma (R3-S2, tonalite), 33.6 ± 1.1 Ma (R6-S19, tonalite), 26.7 ± 1.1 Ma (R1-S15, tonalite) and 24.8 ± 0.8 Ma (R5-S4, granite). Volcanic rocks show ages of 25.7 ± 0.3 Ma (BT16–10, dacite), 29.2 ± 1.4 Ma (R5-S1, andesite), 27.4 ± 0.9 Ma (SG-4, andesite) and 33.6 ± 1.2 Ma (R4-S15, rhyolite). These results indicate that Oligocene magmatism began by 34 Ma and continued at least until 25 Ma (Early to Late Oligocene).

5.2.4. Miocene

We dated sixteen Miocene igneous rocks. Miocene Cu-fertile and barren plutonic rocks have ages of 19.4 ± 0.3 Ma (BT16–3, diorite), 11.9 ± 0.3 Ma (BT16–34, granodiorite), 11.2 ± 0.3 Ma (BT16–28, gabbro), 19.9 ± 0.3 Ma (D19–4, granodiorite), 8.4 ± 0.1 Ma (KR16–33, quartz diorite), 13.3 ± 0.1 Ma (KR16-M2, quartz diorite), 16.9 ± 0.2 Ma (KR16–139, diorite), 8.5 ± 0.1 Ma (KR16-G2, diorite porphyry), 16.7 ± 0.2 Ma (KR16–123, granite), 16.9 ± 0.4 Ma (KR16–140, granite), 12.6 ± 0.1 Ma (KR16–90, granodiorite) and 19.5 ± 0.3 Ma (D19–7, granodiorite). Volcanic rocks show ages of 5.4 ± 0.1 Ma (KR16–2, dacite), 5.5 ± 0.1 Ma (KR16–3, dacite), 6.4 ± 0.2 Ma (KR16–67, dacite) and 10.4 ± 0.2 Ma (KR16–86, dacite). Our data show that Miocene magmatism started by 19.9 Ma and continued until at least 5.4 Ma.

5.2.5. Pliocene-Pleistocene

We analyzed two Pliocene-Pleistocene samples. They have ages of 3.2 ± 0.1 (KR16–87, dacite) and 2.2 ± 0.1 Ma (KR16–88, rhyolite). Compiled data for three other rhyolitic samples indicate zircon U—Pb ages of 1.3 ± 0.1, 2.2 ± 0.1 and 1.2 ± 0.03 Ma (Pang et al., 2016).

5.3. Bulk rock major-trace elements and Sr—Nd isotope

We analyzed Late Cretaceous to Pliocene-Pleistocene magmatic rocks for major- and trace- element abundances (83 samples) and Sr—Nd isotopes (47 samples). New and compiled results are presented in Tables S1 and S2.

5.3.1. Late Cretaceous

Our new and compiled data plotted in $K_2O + Na_2O$ vs SiO_2 diagrams (Fig. 4A–B) show that Late Cretaceous plutonic rocks vary from gabbro to granodiorite whereas volcanic rocks have basaltic to dacitic and trachy-basaltic andesite to trachy-andesitic compositions. Most magmatic rocks have calc-alkaline and high-K calc-alkaline signatures in the K_2O vs SiO_2 diagram (Fig. 4C–D). They have low Sr/Y and $La_{(n)}/Yb_{(n)}$ ratios similar to normal arc rocks (Fig. 4E–H). Late Cretaceous rocks have nearly flat to fractionated REE patterns with $La_{(n)}/Yb_{(n)} = 1$ to 17.5 (Fig. 5A). These rocks are depleted in Nb, Ta and Ti and enriched in Ba, K, Pb, Th and U (Fig. 5B), similar to subduction-related magmatic rocks. Late Cretaceous magmatic rocks have bulk-rock initial $^{87}Sr/^{86}Sr$ and $\varepsilon Nd_{(t)}$ values of 0.7043 to 0.7056 and +7 to +7.5, respectively (Fig. 6E).

5.3.2. Eocene

Eocene plutonic rocks (including lamprophyre dikes) are gabbro-monzogabbro to granite with calc-alkaline to shoshonitic affinities. They are similar to normal arc rocks on Sr/Y and $La_{(n)}/Yb_{(n)}$ plots. Volcanic rocks are trachybasalt-basalt to rhyolite with low-K tholeiite to shoshonitic signatures (Fig. 4A–D). Four samples show high Sr/Y but low $La_{(n)}/Yb_{(n)}$ ratios (Fig. 4E–H). Three samples are similar to adakitic rocks with both high Sr/Y and $La_{(n)}/Yb_{(n)}$ ratios. Eocene igneous rocks are enriched in Ba, U, K and Pb and depleted in Nb, Ta and Ti (Fig. 5C) and in Light REEs (LREEs) compared to HREEs with $La_{(n)}/Yb_{(n)}$ = 1.9–10.6 (Fig. 5D). Eocene magmatic rocks have initial $^{87}Sr/^{86}Sr$ and $\varepsilon Nd_{(t)}$ values of 0.7041 to 0.7055 and +1.9 to +5.4, respectively (Fig. 6E).

5.3.3. Oligocene

Oligocene plutonic rocks range from diorite to granite with calc-alkaline to high-K calc-alkaline and non-adakitic (low Sr/Y and $La_{(n)}/Yb_{(n)}$ ratios) signatures. Volcanic rocks have basaltic to trachytic and rhyolitic compositions that vary from low-K tholeiite to high-K calc-alkaline in the K_2O vs SiO_2 diagram. Oligocene volcanic rocks have non-adakitic signatures (Fig. 4E–G) and LREE enrichment with $La_{(n)}/Yb_{(n)}$ = 2.3–23.8 (Fig. 5E). These rocks show positive anomalies in Ba, Th, U, K and Pb along with negative Nb, Ta, and Ti anomalies (Fig. 5F).

Oligocene rocks are characterized by initial $^{87}Sr/^{86}Sr$ ratio and $\varepsilon Nd_{(t)}$ values of 0.7043 to 0.7073 and − 2.2 to +5.03, respectively (Fig. 6E). However, Asadi (2018) reported more variable $^{87}Sr/^{86}Sr$ ratios and $\varepsilon Nd_{(t)}$ values for Oligocene plutonic rocks from the southeastern UDMB, in the range of 0.7064–0.7093 and − 1.1 to −8.

5.3.4. Miocene

Miocene plutonic rocks have gabbro-diorite to granitic compositions and are mostly calc-alkaline to high-K calc-alkaline in the K_2O vs SiO_2 diagram (Fig. 4D). Most Miocene igneous rocks (especially those host Cu deposits) have high Sr/Y and $La_{(n)}/Yb_{(n)}$ ratios and are adakitic (Fig. 4E–H). Miocene volcanic rocks are basaltic andesite to dacite-trachyte and have calc-alkaline to high-K calc-alkaline affinities. Volcanic rocks have both non-adakitic and adakitic signatures. Miocene

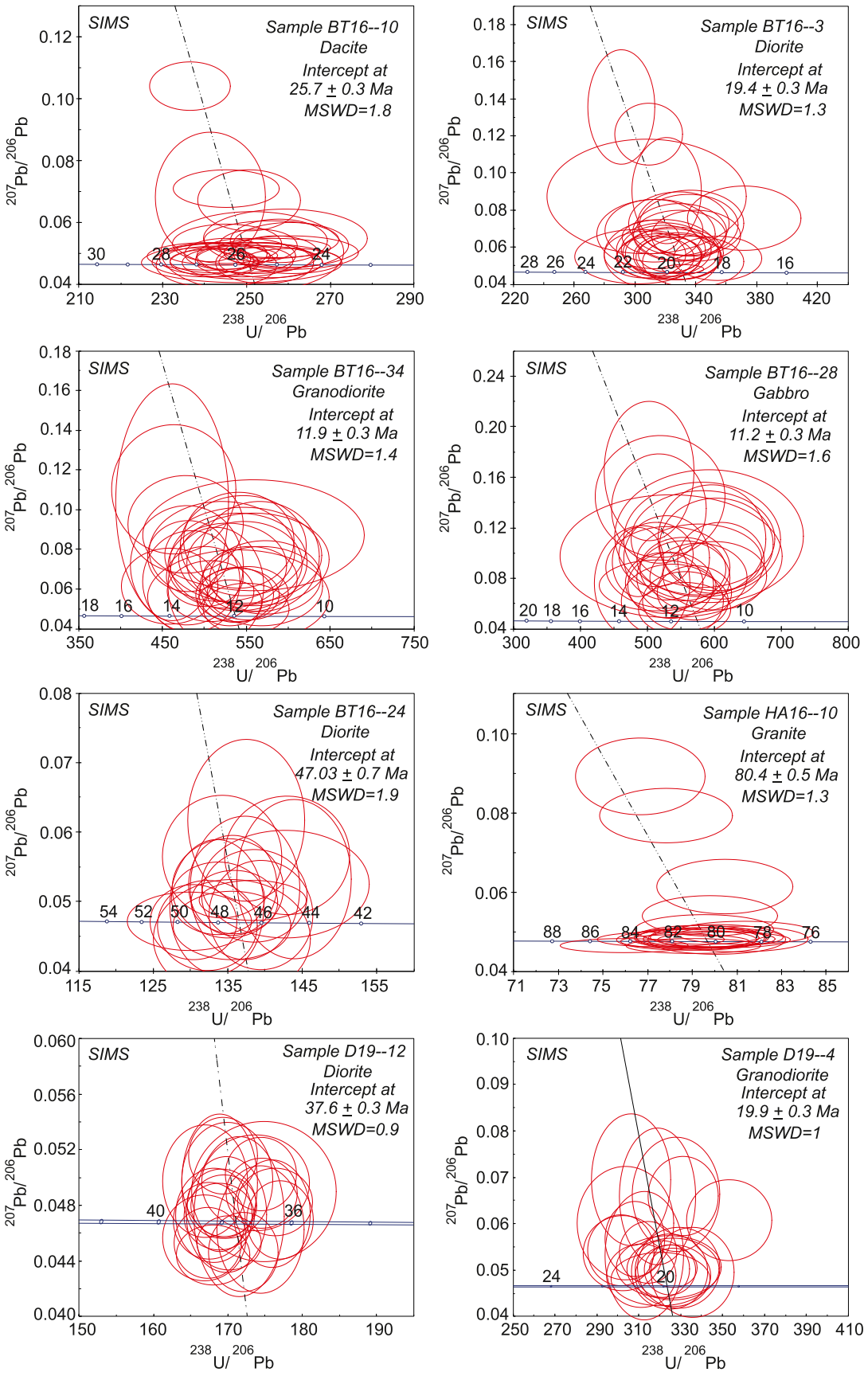

Fig. 2. U—Pb inverse-concordia ($^{207}Pb/^{206}Pb$ vs $^{238}U/^{206}Pb$) SIMS ages for zircons from southeastern UDMB magmatic rocks.

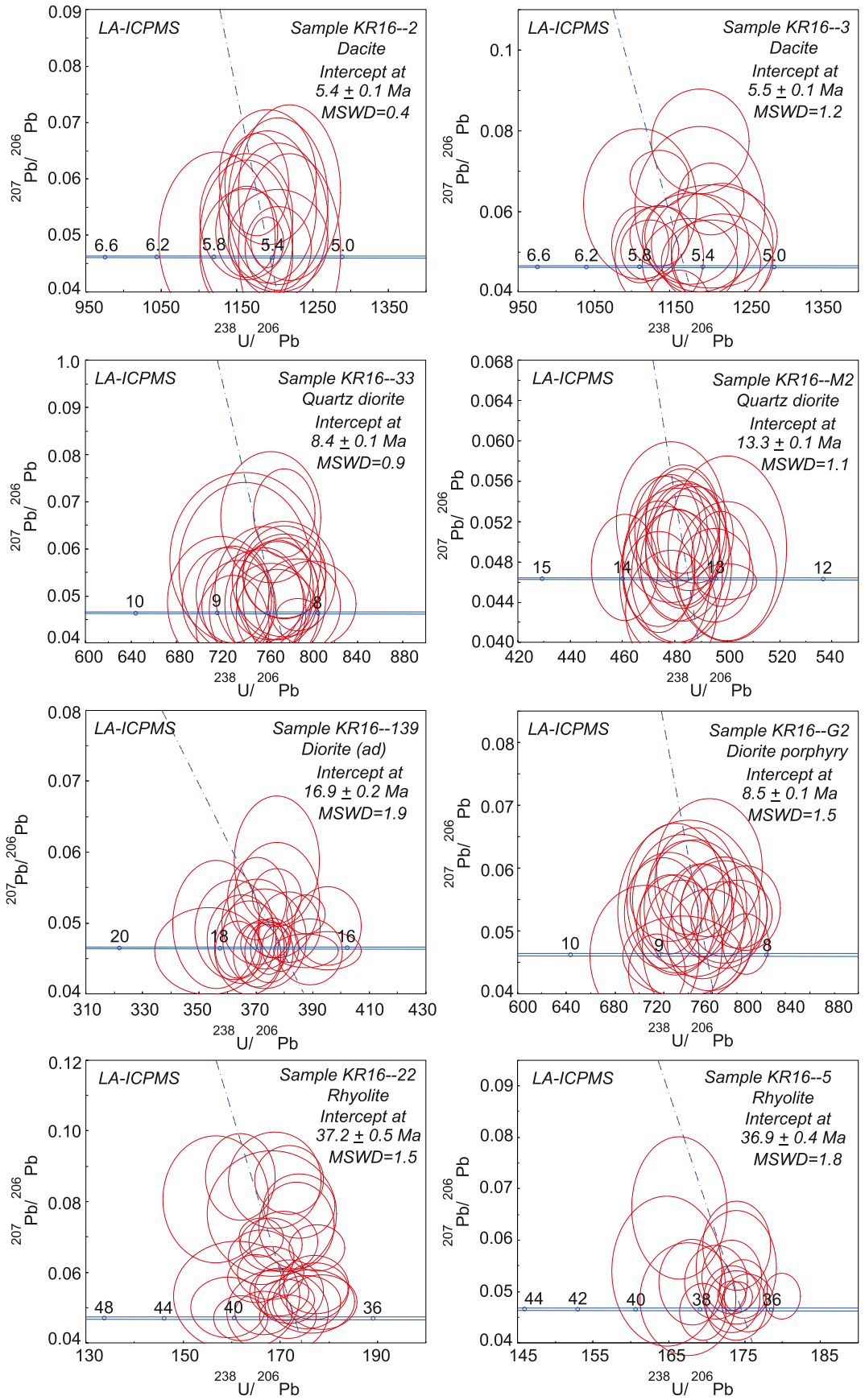

Fig. 3. U—Pb inverse-concordia ($^{207}Pb/^{206}Pb$ vs $^{238}U/^{206}Pb$) LA-ICPMS ages for zircons from southeastern UDMB magmatic rocks.

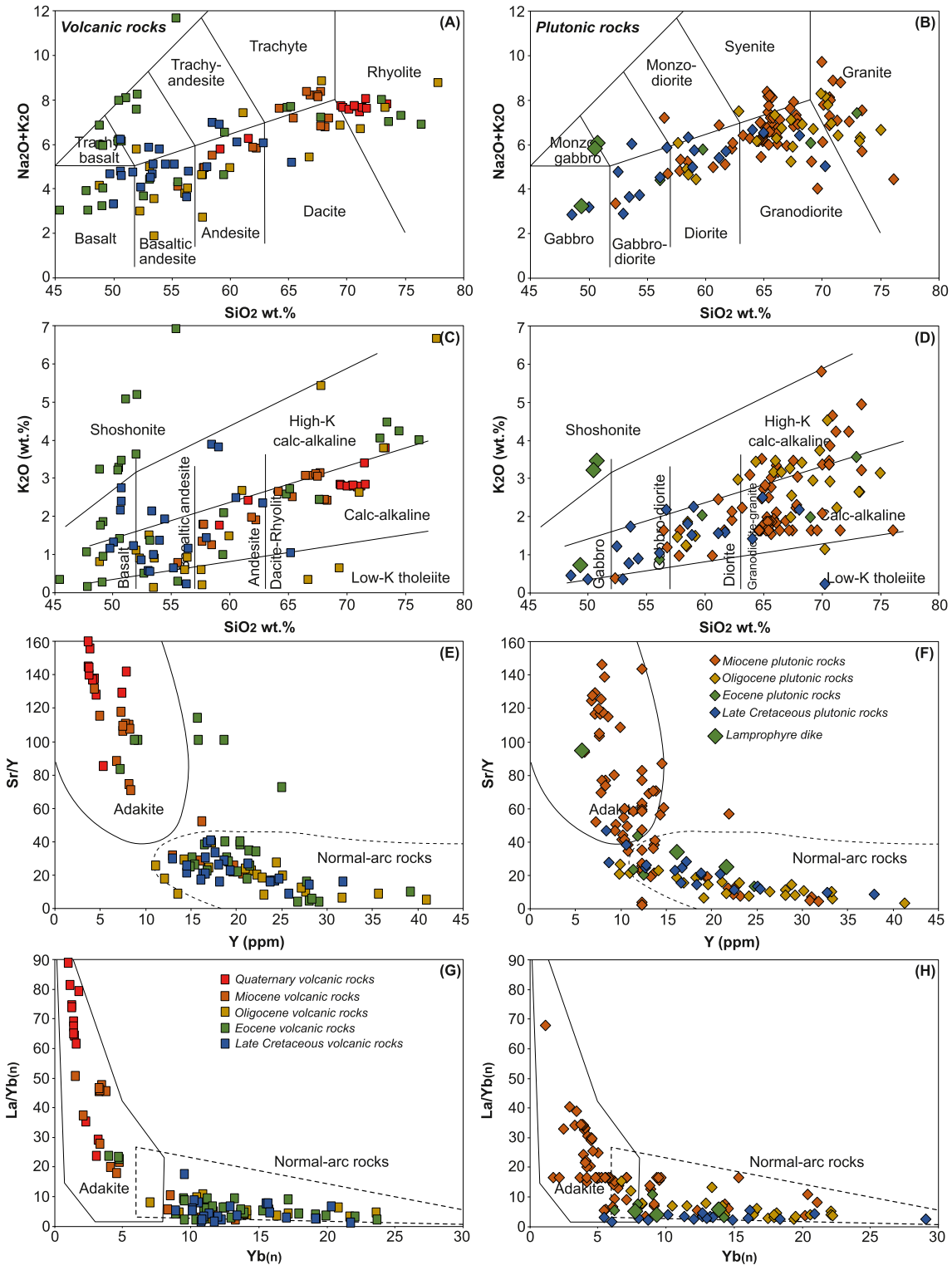

Fig. 4. $Na_2O + K_2O$ and K_2O vs SiO_2 discrimination diagrams for the classification of volcanic (A, C) and plutonic (B, D) rocks from southeastern UDMB. Igneous rocks from different magmatic episodes are represented by distinctive symbols. Sr/Y vs Y and $La_{(n)}/Yb_{(n)}$ vs $Yb_{(n)}$ diagrams for discriminating plutonic (F, H) and volcanic (E, G) rocks from southeastern UDMB (the compositional domains for adakite and normal island-arc dacites and rhyolites are according to Defant and Drummond (1990). For comparison we also plotted data from Asadi (2018), Hosseini et al. (2017), Moghadam et al. (2018), Pang et al. (2016) and Wan et al. (2018).

rocks are enriched in LREEs with $La_{(n)}/Yb_{(n)} = 2.1–67.8$ (Fig. 5G). These rocks are strongly enriched in Ba, Th, U, K and Pb and depleted in Nb, Ta, and Ti (Fig. 5H). Miocene rocks have initial $^{87}Sr/^{86}Sr$ ratios and $\varepsilon Nd_{(t)}$ values of 0.7044 to 0.7057 and −1.5 to +4.2, respectively (Fig. 6E). Similar $\varepsilon Nd_{(t)}$ values of +1.4 to +3.8 (Asadi, 2018), −4.8 to +0.81 (Moghadam et al., 2018) and −0.9 to +3.5 (Wan et al., 2018) are also reported for Miocene plutonic rocks from the southeastern UDMB.

5.3.5. Pliocene-Pleistocene

Pliocene-Pleistocene lavas are andesitic, dacitic and rhyolitic. They

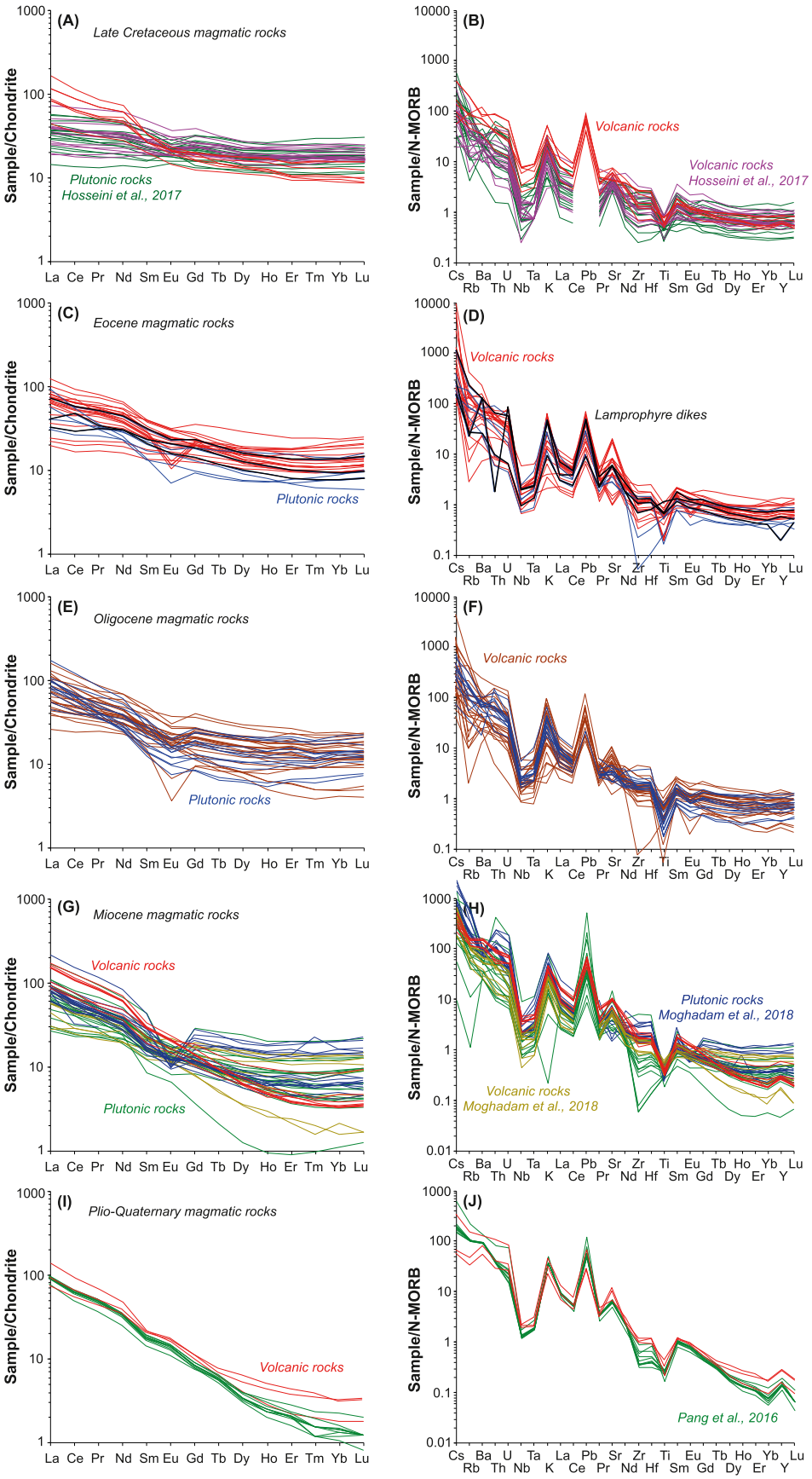

Fig. 5. Chondrite- and N-MORB-normalized REE and trace-element patterns of southeastern UDMB igneous rocks from different magmatic episodes. Normalization data are from Sun and McDonough (1989). For comparison we also plotted data from Hosseini et al. (2017), Moghadam et al. (2018) and Pang et al. (2016).

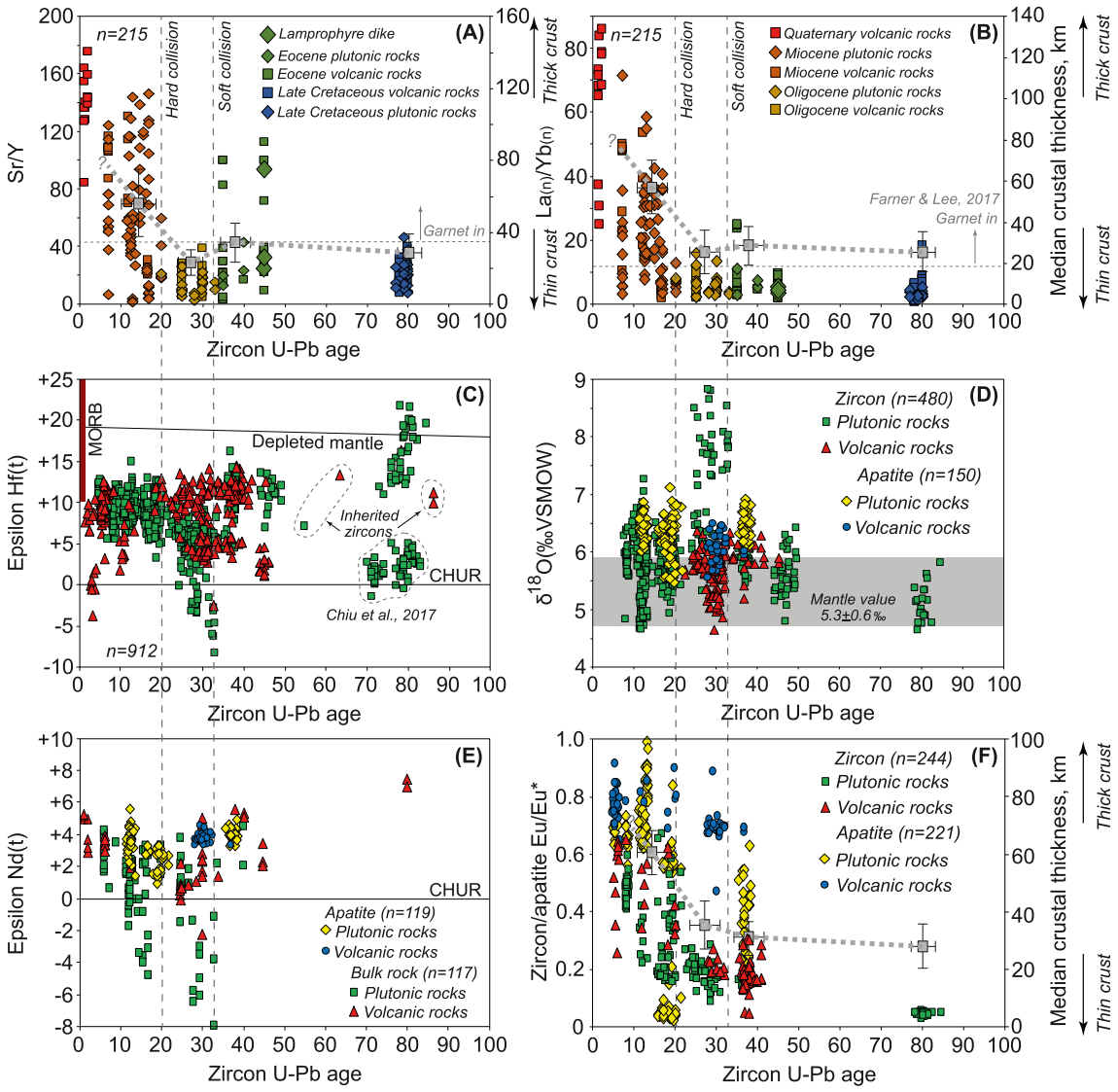

Fig. 6. Plots for bulk rock, zircon and apatite elemental ratios and isotopes of magmatic rocks from the southeastern UDMB. Gray squares with bars in A-B show crustal thickness with standard deviations, calculated using both bulk rock Sr/Y, $La_{(n)}/Yb_{(n)}$ and zircon Eu/Eu* (see text for explanations). The dashed lines show the "soft" and "hard" collision times, which have been adopted from Allen and Armstrong (2008), Mouthereau et al. (2012), Tadayon et al. (2017) and Madanipour et al. (2017), Madanipour et al. (2013), respectively. CHUR = chondrite normalized uniform reservoir; DM = depleted mantle array (based on data from modern Mid-Oceanic Ridge basalts with $^{176}Hf/^{177}Hf$ = 0.28325 and using $^{176}Lu/^{177}Hf$ = 0.0384; Chauvel and Blichert-Toft, 2001). The "garnet-in" dashed lines in A-B are adapted after Farner and Lee (2017).

have high Sr/Y and $La_{(n)}/Yb_{(n)}$ ratios, and are adakitic and are strongly LREE-enriched, with $La_{(n)}/Yb_{(n)}$ = 35.4–89.1 (Fig. 5I). Pliocene-Pleistocene lavas are enriched in Rb, Ba, Th, U, K, Sr and Pb, and are depleted in Nb, Ta, and Ti (Fig. 5J). Pliocene-Pleistocene volcanic rocks have $\varepsilon Nd_{(t)}$ values of +2.9 (*this study*) and + 3.2 to +5.3 (Pang et al., 2016). The initial $^{87}Sr/^{86}Sr$ ratios of these rocks range from 0.7043 to 0.7058.

5.4. Zircon Hf—O isotope and trace elements

Zircon Hf—O isotopic data for southeastern UDMB igneous rocks are summarized in Fig. 6C–D and Tables S6–S8, whereas zircon trace-elements data are summarized in Table S5. For zircon trace elements, we used criteria proposed by Lu et al. (2016) to exclude contaminated (with inclusions) analyses, e.g., La >1 ppm is considered to show apatite contamination, Fe > 5000 ppm is taken to reflect contamination by Fe oxides and Ti >50 ppm reveals contamination by Ti—Fe oxides.

5.4.1. Late Cretaceous

Zircon initial $\varepsilon Hf_{(t)}$ values range from +10 to +21.6 (Fig. 6C), whereas zircon $\delta^{18}O$ varies between 4.6 and 5.8‰ (Fig. 6D). These $\delta^{18}O$ values are similar to those reported for mantle-derived rocks (5.3 ± 0.6; Valley et al., 1998). In addition, Chiu et al. (2017) reported zircon $\varepsilon Hf_{(t)}$ values of −1.5 to +15.2 for Late Cretaceous magmatic rocks of the southeastern UDMB. Late Cretaceous zircons are characterized by steep patterns from heavy REE (Lu) to light REE (Ce) (Fig. S2), with average $Ce_{(n)}/Lu_{(n)}$ = 0.0004, $Dy_{(n)}/Yb_{(n)}$ = 0.14 and a strong negative anomaly in Eu ($Eu_{(n)}/Eu_{(n)}^*$ = 0.04) (Fig. 6F).

5.4.2. Eocene

Zircon $\varepsilon Hf_{(t)}$ and $\delta^{18}O$ values for Eocene rocks vary from +3.3 to +16.1 and 8.4 to 4.8‰, respectively (Fig. 6C–D). Our data are consistent with reported $\varepsilon Hf_{(t)}$ data for Eocene magmatic rocks of the southeastern UDMB which range from +1.1 to +14.5 (Chiu et al., 2017). Eocene zircons have steep patterns from HREEs to LREEs with average $Ce_{(n)}/Lu_{(n)}$ = 0.004, $Dy_{(n)}/Yb_{(n)}$ = 0.16 and depletion in Eu ($Eu_{(n)}/Eu_{(n)}^*$ =

0.18) (Fig. 6F).

5.4.3. Oligocene

Zircon $\varepsilon Hf_{(t)}$ values for Oligocene rocks vary from −2.6 to +14.1 (Fig. 6C), whereas zircon $\delta^{18}O$ varies between 4.7 and 9.1‰ (Fig. 6D). In addition, $\varepsilon Hf_{(t)}$ values of +2.6 to +10.6 and − 10.6 to +2.8 are reported for zircons from Oligocene plutonic rocks by Chiu et al. (2017) and Asadi (2018), respectively. Zircon $\delta^{18}O$ values vary between 6.3 and 9.4 for Oligocene barren rocks (Asadi, 2018). Oligocene zircons are also represented by a steep trend from HREEs to LREEs with average $Ce_{(n)}/Lu_{(n)} = 0.004$, $Dy_{(n)}/Yb_{(n)} = 0.17$ and depletion in Eu ($Eu_{(n)}/Eu_{(n)}^* = 0.19$) (Fig. 6F).

5.4.4. Miocene

Zircon $\varepsilon Hf_{(t)}$ values for Miocene rocks varies between +1.8 and + 14.9 (Fig. 6C), whereas zircon $\delta^{18}O$ varies between 4.7 and 7.3‰ (Fig. 6D). These values are similar to those reported by Chiu et al. (2017) (+6.1 to +12.7) and Asadi (2018) (+6.1 to +10.6) for Miocene plutonic rocks. Zircon $\delta^{18}O$ values vary from 5.1 to 6.8‰ for Miocene fertile rocks (Asadi, 2018). Miocene zircons have a less steep trend from HREEs to LREEs with average $Ce_{(n)}/Lu_{(n)} = 0.01$, moderate $Dy_{(n)}/Yb_{(n)} = 0.15$ and less Eu depletion ($Eu_{(n)}/Eu_{(n)}^* = 0.39$) compared to Late Cretaceous to Oligocene zircons (Fig. 6F). Miocene zircons have also a higher positive Ce anomaly than Late Cretaceous to Oligocene zircons.

5.4.5. Pliocene-Pleistocene

Zircon $\varepsilon Hf_{(t)}$ values for Pliocene-Pleistocene lavas vary from −3.8 to +10.4 (Fig. 6C).

5.5. Apatite major and trace elements and O-Sr-Nd isotopes

Apatite is the dominant phosphorus-bearing mineral in calc-alkaline rocks and also concentrates REEs, Th and *U. Major*-trace elements and O-Sr-Nd isotope composition of apatites are useful for understanding the geochemical evolution of magmas, the genesis of various type of granites and mechanisms of Cu mineralization (Palma et al., 2019; Sha and Chappell, 1999). Major- and trace- element compositions of apatite are sensitive to changes in magmatic composition (including magmatic fractionation) and oxidation state (e.g., Belousova et al., 2002b; Cao et al., 2012; Duan et al., 2019; Pan et al., 2020; Sha and Chappell, 1999; Yang et al., 2018). Apatites that crystallize from oxidized magmas should contain more Eu but less Ce, Ga, and Mn, compared with apatites that crystallize from less oxidized magmas.

We selected Eocene (sample D19–12), Oligocene (sample R5-S1) and Miocene barren (samples D19–4 and D19–7) to fertile rocks (samples KR16–71, KR16–33, KR16-M2, KR16–3 and KR16–67) for the analysis of apatite major- and trace-elements and O-Sr-Nd isotopes. Magmas with high SiO_2 contents ($SiO_2 > 70$ wt%) and/or peraluminous melts (S-type) have different effects on the solubility of apatite in magmas and its composition (Palma et al., 2019; Sha and Chappell, 1999). Our samples from southeastern UDMB are metaluminous and samples selected for apatite analysis have $SiO_2 < \sim 66$ wt%. Therefore, the difference in apatite trace elements between our samples is not influenced by high alumina saturation indices (e.g., apatite from S-type granites) and/or extreme fractionation. The major-element (e.g., MnO) composition of apatites from southeastern UDMB show no correlation with the aluminium saturation index (ASI) or SiO_2 (the fractionation index) of host magmas (*not shown*).

Apatites from Eocene rocks have $\delta^{18}O = 6.50 \pm 0.27$‰, and Oligocene apatites have $\delta^{18}O = 6.08 \pm 0.30$‰. Apatites from both fertile and barren Miocene rocks have similar $\delta^{18}O$ of 6.43 ± 0.32‰ and 6.25 ± 0.30‰, respectively. Apatites are both Cl- or F-rich; Oligocene apatites and those from fertile Miocene sample KR16-M2 have high Cl >2 wt%, but most apatites from Miocene fertile rocks as well as Eocene apatites have low Cl contents. Barren Miocene rocks have Cl contents between those of Oligocene and sample KR16-M2 apatites and Eocene and fertile rocks. The high Cl content of apatites from sample KR16-M2 compared to those from the other fertile magmatic rocks suggests that its melt was more Cl-rich as apatite crystallized. In addition, hydrothermal exsolution may have led to loss of Cl in apatite from other fertile magmatic rocks (Boudreau and Kruger, 1990; Meurer and Boudreau, 1996; Schisa et al., 2015). Exsolution of Cl- bearing fluids would extract Cu from the melt in the form of Cl-bearing complexes (Williams et al., 1995). Apatite from Miocene fertile rocks is slightly depleted in MnO compared to other rocks; MnO changes from 0.03 to 0.18 wt% (mean 0.11 ± 0.03) for Miocene fertile rocks, whereas Eocene apatites have MnO = 0.04 to 0.17 wt% (mean 0.10 ± 0.02) and Oligocene apatites are represented by MnO = 0.09–0.22 wt% (mean 0.15 ± 0.03). Apatite from Miocene barren rocks has higher MnO = 0.06–0.19 wt% (mean 0.14 ± 0.02). The lower MnO of apatite from fertile rocks may be related to the oxidized nature of fertile, Cu-bearing magmas and thus the predominance of highly-charged Mn (Mn^{+4} and Mn^{+6}), which cannot replace Ca^{+2} in the apatite structure (Sha and Chappell, 1999). Instead, in oxidized magmas, V occurs as V^{+5}, which can form VO_4^{3-} and thus can substitute for PO_4^{3-} in apatites.

Eocene apatites show a steep trend from LREEs to HREEs with average $La_{(n)}/Yb_{(n)} \sim 77$ and Eu depletion ($Eu_{(n)}/Eu_{(n)}^* = 0.4$) (Fig. S3); the trend from La to Sm ($La_{(n)}/Sm_{(n)} = 11.9$) is steeper than in other analyzed apatites. Oligocene apatites have less steep LREE to HREE patterns and less Eu depletion with $La_{(n)}/Yb_{(n)} = 53.2$, $La_{(n)}/Sm_{(n)} = 4.2$ and $Eu_{(n)}/Eu_{(n)}^* = 0.7$. Miocene barren rocks have $La_{(n)}/Yb_{(n)} = 20.5$, $La_{(n)}/Sm_{(n)} = 2.9$ and $Eu_{(n)}/Eu_{(n)}^* = 0.3$, whereas fertile rocks have $La_{(n)}/Yb_{(n)} = 56.7$, $La_{(n)}/Sm_{(n)} = 6.5$ and $Eu_{(n)}/Eu_{(n)}^* = 0.8$. There are two non-equivalent sites for Ca^{+2} in apatite, which Eu^{+3}, the cation with similar ionic radius to Ca^{+2} and abundant in oxidized magmas, can easily occupy these non-equivalent sites compared to Eu^{+2} (Sha and Chappell, 1999). Sample KR16-M2 displays chondrite-normalized spoon-shaped MREE-HREE trend compared to apatites from other fertile rocks, which could suggest extreme amphibole fractionation (Fig. S3). We also analyzed for in situ Sr—Nd isotopes in the larger apatites; most are too small for a laser spot size of 60–120 μm needed. Apatite $\varepsilon Nd_{(t)}$ values changes from +0.9 to +3.2 for Miocene barren rocks, to +1.4 to +5.5 for Miocene fertile rocks, +3.2 to +4.8 for Eocene rocks and + 3.3 to +4.5 for Oligocene rocks (Fig. S7). Miocene fertile rocks have lower $^{87}Sr/^{86}Sr$ values than other rocks, ranging from 0.70478 to 0.70450, compared to 0.70596–0.70449 for Eocene rocks and 0.70542–0.70464 for Oligocene rocks. Apatite from Miocene barren rocks (sample D19–7) have high $^{87}Sr/^{86}Sr = 0.70802$–$0.70607$. Apatite from sample D19–4 is too small for a laser spot after ablating the grains for trace elements and Nd isotopes.

6. Discussion

Four questions concerning southeastern UDMB arc magmatism are addressed below. First, we discuss the timescale of magmatism along the magmatic front and its relations to back-arc magmatism. Second, we discuss the time-dependant geochemical variations of magmatic rocks and explore the significance of this for reconstructing crustal thickness. Third, we consider what geochemical variations can be identified during the transition between the initial Arabia-Iran collision and post-initial collisional period? Fourth, we examine what are the relationships between zircon and apatite compositions and Cu mineralization?

6.1. Timescale of magmatism

Our new data coupled with previously published ages allow southeastern UDMB magmatism to be subdivided into two distinct episodes: ~80–70 Ma and ~ 50–1.2 Ma (Eocene to Pleistocene) (Fig. S8). We assume that the magmatic flux we discuss in this paper was proportional to the number of rock ages. We recognize that identifying magmatic flare-ups and lulls only from compiled zircon age peaks can introduce bias because younger rocks may be oversampled and because most

Eocene rocks are zircon-poor intermediate to mafic volcanic rocks. We have attempted in our sampling program to counteract these possible biases.

Assuming that the magmatic flux is approximated by the number of rock ages, the high-flux magmatic episode that started at ~40 Ma intensified after the collision with Arabia began ~32 Ma, without further magmatic lulls until very recently. Our data do not confirm the Early to Late Eocene flare-up nor the Middle Oligocene to Early Miocene magmatic lull in the southeastern UDMB proposed by Verdel et al. (2011). Our compiled data also confirm that there are differences in magmatic flux between the southeast and central segments of the UDMB (the magmatic front) and between the UDMB and magmatic back-arc. For example, Late Cretaceous magmatic rocks are absent in central UDMB, but Early Eocene (~50 Ma) to Early Miocene (~20 Ma) igneous rocks are abundant. Furthermore, compared to the UDMB, Late Cretaceous magmatism was concentrated in the Birjand-Zahedan and/or Sabzevar-Torud magmatic back-arc. Magmatism in the Alborz-Azerbaijan magmatic belt was vigorous from ~70 to 30 Ma, with a flare-up at 60–40 Ma, which is consistent with new $^{40}Ar—^{39}Ar$ ages for Alborz-Azerbaijan volcanic rocks (~45 to 36 Ma; van der Boon et al., 2021) and zircon U—Pb and biotite $^{40}Ar—^{39}Ar$ ages for pyroclastic rocks of the Eocene Karaj Formation of central Alborz (49.3 ± 2.9, 45.3 ± 2.3 and 41.1 ± 1.6 Ma; Verdel et al., 2011, and younger ages of 36.0 ± 0.2 Ma; Ballato et al., 2011). Our data show that the high magmatic fluxes in the Alborz-Azerbaijan magmatic belt started earlier (~60 m.yr. earlier than considered by Verdel et al., 2011). The compiled data also show that the rate of magmatic activity decreased in the back-arc after collision with Arabia began ~32 Ma (Fig. S8).

6.2. Temporal variations in magmatism and crustal thickness

Our geochemical and isotopic data reveal systematic temporal variations for Late Cretaceous to Pleistocene magmatic rocks, although these all show the geochemical signatures expected for melts generated above subduction zones, i.e., depletion in Nb—Ta and enrichment in Rb, Ba, Th, U and Pb (Fig. 5). In detail, Late Cretaceous rocks have low Sr/Y and La/Yb and mantle-like zircon O—Hf and bulk-rock Nd isotopes (Fig. 6A–E). Some Late Cretaceous diorites and granodiorites have less radiogenic zircon $\varepsilon Hf_{(t)}$ values (Chiu et al., 2017). Eocene magmatism was geochemically variable, with mostly low but some high Sr/Y and La/Yb ratios as well as broadly similar zircon O—Hf isotopic values. Some Eocene volcanic rocks are shoshonitic (Fig. 4C–D). Oligocene rocks have similar Sr/Y and La/Yb to Eocene rocks but more variable $\delta^{18}O$ and zircon $\varepsilon Hf_{(t)}$ as well as bulk-rock $\varepsilon Nd_{(t)}$ values. Miocene (20–5.3 Ma) rocks show increasing Sr/Y and La/Yb, indicating the increasingly adakitic nature of magmatism at this time. These rocks are broadly similar to older rocks in terms of zircon $\delta^{18}O$ and $\varepsilon Hf_{(t)}$ and bulk-rock $\varepsilon Nd_{(t)}$. Pliocene-Pleistocene rocks have high Sr/Y and La/Yb with bulk-rock $\varepsilon Nd_{(t)}$ and zircon $\varepsilon Hf_{(t)}$ values that are mostly radiogenic, but some also show less radiogenic Hf, suggesting contamination with upper continental crust (Fig. 6). These geochemical data show that southeastern UDMB magma-genetic system changed from Late Cretaceous calc-alkaline to increasingly adakitic Neogene magmatism when the "hard" collision with Arabia began at ~20 Ma. Our zircon O—Hf and bulk-rock Nd isotopic results indicate that Early Oligocene and Early Miocene (32–20 Ma) magmatism was isotopically more variable than younger magmatism and became more radiogenic with time. Most Early to Late Miocene (<20 Ma) magmatic rocks from the southeastern UDMB have radiogenic $\varepsilon Hf_{(t)}$ values (> + 5, Fig. 6C) and show more homogeneous isotopic compositions than Late Cretaceous (~80 Ma) to Early Miocene (~20 Ma) rocks. Bulk-rock Nd-isotope data reveal some similarities in magmatic sources of Eocene-Pleistocene rocks. These rocks are isotopically different from melts expected from a depleted MORB mantle (DMM) and/or depleted mantle beneath the Pacific arcs, but mostly show similarities to the melts deriving from a highly refertilized mantle lithosphere. Most Eocene-Pleistocene rocks plot in a trend between the average fertilized sub-continental lithospheric mantle (Griffin et al., 1988; O'Reilly and Griffin, 2013) and the subducting sediment melts or global subducting sediments (GLOSS) in the plots of $\varepsilon Nd_{(t)}$ vs $^{87}Sr/^{86}Sr$ and $\varepsilon Nd_{(t)}$ vs elemental ratios such as Th/Nd, Hf/Nd and Sm/Nd (Fig. S4). However, some rocks plot in a trend between the average fertilized sub-continental lithospheric mantle (e.g., Griffin et al., 1988; O'Reilly and Griffin, 2013) and upper continental crust of Iran (Moghadam et al., 2021). Igneous rocks that interacted with the Cadomian continental crust of Iran, such as Oligocene *syn*-collisional magmas, show less radiogenic whole-rock Nd and zircon Hf and high $\delta^{18}O$ values. Late Cretaceous rocks with more radiogenic Nd and zircon Hf isotopes probably reflect derivation from a depleted mantle isotopically similar to DMM.

Sr/Y and REE patterns (e.g., La/Yb) provide information about the role of pressure-sensitive residual or fractionating minerals such as plagioclase and garnet or amphibole, and serve as first-order constraints on depths of magma generation and fractionation and indirectly on crustal thicknesses (Lieu and Stern, 2019; Profeta et al., 2015). Lower La/Yb (<15) and Sr/Y (<40) generally indicate residues dominated by plagioclase and/or clinopyroxene; higher Sr/Y (>40) and La/Yb (> 30) reflect retention of HREE by garnet and/or amphibole in the residues or cumulates (e.g., Barth et al., 2002; Farner and Lee, 2017). To understand temporal geochemical variations in the southeastern UDMB and their causes, crustal thickness has been reconstructed by using Sr/Y and La/Yb elemental ratios for intermediate to felsic rocks (55–68 wt% SiO_2) (Chapman et al., 2015; Farner and Lee, 2017; Hou et al., 2015a; Hu et al., 2020; Hou and Zhang, 2015; Lieu and Stern, 2019; Profeta et al., 2015). For reasonable thickness estimates, we have ignored Eocene lamprophyre dikes and some Eocene volcanic rocks with high calc-alkaline affinities. This is because the alkalinity would affect the thickness estimates (Hou et al., 2015b; Hu et al., 2020). Also, we do not estimate crustal thicknesses for Pliocene-Pleistocene rocks based on the geochemical data since these rocks are highly silicic and/or show extremely high Sr/Y (and/or $La_{(n)}/Yb_{(n)}$) ratios, well outside the range of calibrated paleomohometric sensors (Profeta et al., 2015).

These proxies indicate that crustal thicknesses increased after collision between Iran and Arabia began; the continental crust was at least 20–30 km thicker than before collision (Fig. 6A–B)– and this can be confirmed from plots of La/Yb and Dy/Yb vs SiO_2 (Fig. S5). These plots show that igneous rocks from each age group experienced mostly clinopyroxene + plagioclase- or amphibole-dominated fractionation. However, Miocene and Pleistocene high-Sr/Y rocks display trace of high-pressure garnet and or amphibole fractionation. Garnet and/or amphibole fractionation, along with assimilation and fractional crystallization (AFC) processes, at the base of the thickened continental crust are thought to be responsible for the genesis of some adakitic rocks (e.g., Chiaradia, 2009; Hidalgo and Rooney, 2014). In addition, zircon $Eu/Eu^*_{(n)}$ ratios in intermediate to felsic rocks correlate with bulk rock La/Yb and can also be used to infer crustal thickness (Tang et al., 2021; Tang et al., 2020a). These estimates based on the zircon $Eu/Eu^*_{(n)}$ ratios have been confirmed by results presented by (Balica et al., 2020). Our results show that zircon $Eu/Eu^*_{(n)}$ increases with time (Fig. 6F), consistent with the trend of high Sr/Y and La/Yb in bulk rocks and crustal thickening during collision.

6.3. Zircon-apatite composition and Cu mineralization

In situ trace-element analyses of zircon reflect the chemistry of the host magmas (Belousova et al., 2002c). Studies on Tibetan Cu deposits have shown that zircon in mineralized rocks has higher $(Eu/Eu^*)/Y$ than in barren rocks, suggesting the source fertility controls the genesis of mineralization (Lu et al., 2016). Apatite is also sensitive to geochemical changes in magmatic systems and can be used to understand the Cu fertility of host magmas (Palma et al., 2019). The trace-element contents of apatite are mainly controlled by (1) their abundance in the magma at the time of apatite crystallization, which can be modified by an earlier

fractionating mineral (e.g., plagioclase, zircon, allanite, monazite etc., Duan et al., 2019); and (2) the partition coefficients between apatite and melt, which are mainly controlled by magma composition (e.g., SiO_2, Cl, F content), degree of differentiation and P-T conditions (Li and Hermann, 2017; Prowatke and Klemme, 2006; Watson and Green, 1981). Measured $^{87}Sr/^{86}Sr$ and $^{143}Nd/^{144}Nd$ isotope ratios of apatite could be further used to infer the composition of host magmas (Belousova et al., 2002c; Palma et al., 2019). Most zircons in Miocene adakitic rocks from the southeastern UDMB show high Hf/Y (> ~ 10 to <70) and $Eu/Eu^*_{(n)}$ (> ~ 0.3) but low Yb/Gd (<~30) (Fig. S6), which represent fractionation of amphibole (±titanite) and/or garnet from host magmas (e.g., Lu et al., 2016). Zircon $Eu/Eu^*_{(n)}$ is high in fertile, Cu-bearing Miocene rocks. This ratio also increases with time, consistent with the trend of high Sr/Y and La/Yb in bulk rocks and thickening of the crust after collision (Deng et al., 2018; Tang et al., 2020b).

Apatites from Miocene barren and fertile rocks as well as Eocene-Oligocene rocks can provide further information about the Cu fertility of host magmas. Apatites $\delta^{18}O$ values are similar to zircon $\delta^{18}O$ and show no obvious trend with age (Fig. 6D). However, apatite in fertile Tibetan rocks has high Cl and S concentrations with high Cl/F and V/Y and less radiogenic Sr isotopes than in barren rocks (Xu et al., 2021), suggesting derivation of volatile-rich magmas from metasomatized SCLM. Our dataset shows that apatites from fertile UDMB Miocene rocks have high Sr/Y and $Eu/Eu^*_{(n)}$ (Fig. 7). However, our sample from Cu-bearing rocks of NE Shahr-e-Babak (sample KR16-M2, Fig. 1B) shows a different trend and is characterized by high $Eu/Eu^*_{(n)}$ but instead low Sr/Y. The crystallization of plagioclase prior to or during apatite saturation would significantly deplete the melt in Eu and Sr simultaneously, generating a negative Eu anomaly and decreased Sr content. Thus, the Eu/Eu* should correlate with the Sr contents. The Cl, F, S concentrations and V/Y ratios behave differently; in most fertile rocks from the southeastern UDMB, e.g., apatites have high F contents and V/Y ratios but low Cl contents. Instead, apatites from sample KR16-M2 have high Cl and S (SO_3 > 0.2), but low F contents. Apatite $Eu/Eu^*_{(n)}$ and Sr/Y ratios are low in Eocene and Oligocene rocks as well as in Miocene barren rocks. V/Y is highly variable but also is higher in Eocene and Oligocene rocks

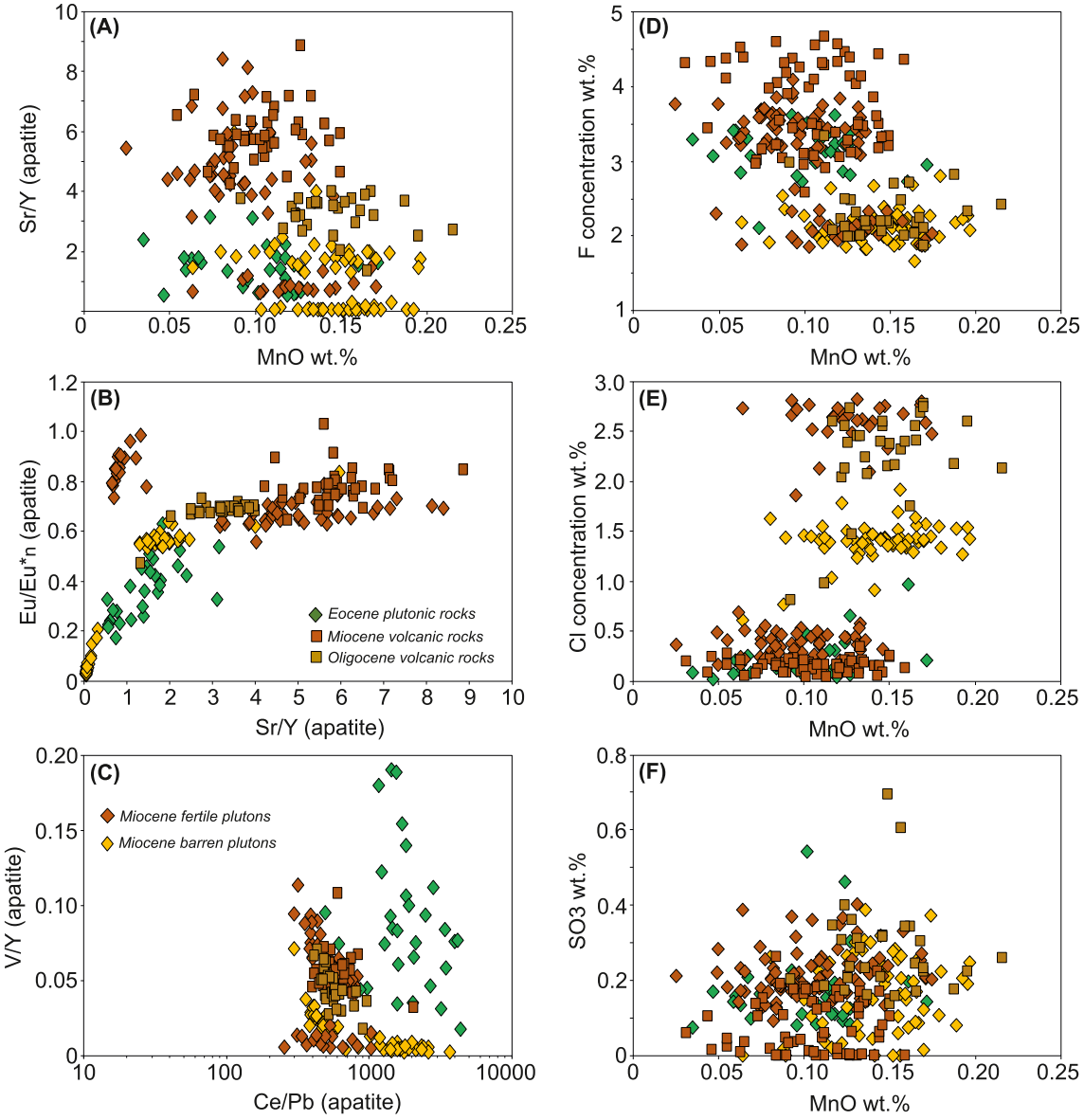

Fig. 7. Sr/Y vs MnO (*wt*%) (A), $Eu/Eu^*_{(n)}$ vs Sr/Y (B), V/Y vs Ce/Pb (C), fluorine (*wt*%) vs MnO (D), chlorine (*wt*%) vs MnO (E) and SO_3 (*wt*%) vs MnO (F) compositional variation diagrams for apatite grains from southeastern UDMB igneous rocks. MnO, F, Cl and SO3 have been analyzed by Electron Microprobe whereas trace elements such as Eu, Gd, Sm, V, Y, Ce and Pb have been analyzed using Laser Ablation Inductively Coupled Plasma-Mass Spectrometry (see text for explanations).

than in Miocene barren rocks. The lower V/Y ratio in apatite of sample KR16-M2 could be related to extreme amphibole fractionation during apatite crystallization. The partition coefficient (D) of Y in amphibole is higher than V. However, in the halogen-bearing felsic and oxidized magmas, such as those that trigger Cu mineralization, the $D^{amphibole/melt}$ for Y depends on the Mg# of fractionating amphibole, changing from D > 26 for amphibole with Mg# = 0.63 to D ~ 0.75 when Mg# = 0.82 (Iveson et al., 2018). This means that fractionation of magnesium-rich amphiboles in an oxidizing magma could be responsible for enriching Y in the melt from which apatite crystallizes (i.e., sample KR16-M2).

On the other hand, the positive correlation between apatite Eu/Eu* and Sr of some Miocene barren rocks (Fig. S9) could indicate control of magmatic Eu via feldspar crystallization (Pan et al., 2020). The Eu/Eu* vs Sr plot for sample KR16-M2 also displays a weak positive trend (Fig. S9), which suggests feldspar fractionation during apatite crystallization. In addition, the La/Sm, Ce/Th and Y/ ΣREE ratios of apatite are linked to the oxygen fugacity of the magma (Belousova et al., 2002a). La/Sm and Ce/Th increase with increasing oxygen fugacity, whereas Y/ ΣREE shows a negative correlation with oxygen fugacity. These correlations may reflect the stabilisation of minor phases such as allanite along with apatite, that both take up Fe^{3+} and compete with apatite for the HREE (Belousova et al., 2002a). The fertile rocks from southeastern UDMB have apatites with higher La/Sm and lower Y/ ΣREE compared to other apatites, implying higher oxygen fugacity. However, the Ce/Th and La/Sm ratios of apatites from sample KR16-M2 are abnormally low. The low Ce/Th and La/Sm ratios of the KR16-M2 apatites along with high Y/ ΣREE suggests lower oxygen fugacity for this sample, compared to other Miocene fertile apatites, whereas crystallization of plagioclase prior to or during apatite crystallization depletes the melt in Eu and Sr simultaneously, producing a positive correlation in plots of Eu/Eu*, $La_{(n)}/Yb_{(n)}$ and/or Sr/Y vs Sr for sample KR16-M2 (Fig. S9). Low oxygen fugacity (along with fractionation of magnesium-rich amphiboles) is also consistent with the low V/Y ratio of this samples.

Apatite $Eu/Eu^*_{(n)}$ increases with time, although barren Miocene rocks have low $Eu/Eu^*_{(n)}$ (Fig. 6F). There is no increase in SO_3 in apatites with decreasing age, in contrast to the clear trend in apatite S with age in Tibet (Tang et al., 2020b). This probably indicates there was only minor fractionation of garnet during the crustal thickening beneath the southeastern UDMB. There is no noticeable trend in apatite Nd isotopes; fertile rocks generally have more radiogenic Nd, but less radiogenic Sr than Eocene-Oligocene rocks as well as Miocene barren rocks (Fig. 6E, Fig. S7). Porphyry Cu deposits are considered to have formed by magmas that were oxidized and unusually rich in Cu (e.g., Halter et al., 2005; Richards, 2015; Stern et al., 2007), but also need sulfides to not be saturated and separate from the magma before exsolution of magmatic fluids (Hou et al., 2020). These considerations lead us to assume that the Miocene fertile magmas had higher magmatic oxygen fugacity, which promoted the decomposition of sulfides in the magma source to form parental magmas rich in S and Cu. Lower oxygen fugacity in Eocene-Oligocene magmas not only delayed the melting of sulfides from the sources but also facilitated the early saturation of the Cu-bearing sulfide during fractional crystallization (Wang et al., 2014). This could produce sulfide-rich magmatic cumulates at the base of lower-crustal magma chambers, rather than high-level Cu porphyries.

6.4. Formation of Cu deposits in southeastern UDMB

Several mechanisms have been suggested for forming Cu deposits in Iran (see Deng et al. (2018), Wan et al. (2018) and Atapour and Aftabi (2021) and references therein). Southeastern UDMB Cu-bearing rocks are Miocene and have high Sr/Y ratios with radiogenic bulk-rock Nd and zircon Hf isotopes, "mantle" $\delta^{18}O$ and higher zircon Eu/Eu*, similar to fertile adakitic rocks worldwide (Hollings et al., 2005; Hou et al., 2015a; Hou and Zhang, 2015; Lu et al., 2016; Stern et al., 2011; Wang et al., 2018). Asadi (2018) suggested that the Cu-barren rocks are of Eocene to Oligocene age and have unradiogenic bulk-rock Nd and zircon Hf signatures whereas Cu-bearing, fertile rocks have radiogenic Nd and Hf isotopes and come from melting of a more juvenile source. However, our results indicate that similarly-aged barren and fertile rocks in the southeastern UDMB have identical bulk-rock Nd and zircon Hf-isotope signatures, although other parameters such as zircon Hf/Y and Eu/Eu* and apatite Eu/Eu* and Sr/Y differ. Apatite compositions show that there might be multiple mechanisms for forming Cu deposits and/or that the composition of Cu-bearing fluids (halogen complexes) was different.

The major models suggested for making Miocene Cu deposits in southeast Iran include: (i) partial melting of metasomatized SCLM, and (ii) melting of lower continental crust (Aghazadeh et al., 2015; Wan et al., 2018). It is supposed that melting of SCLM refertilized by volatile-enriched magmas/fluids due to subduction modification or accompanying asthenosphere upwelling can play a vital role in generating magmatic-hydrothermal ore systems (e.g., Hou et al., 2015a; Hou et al., 2015b; Hronsky et al., 2012; Richards, 2009). Furthermore, asthenosphere upwelling can also modify the mantle lithosphere particularly above subduction zones, with the subducting slab supplying fluids/melts. These magmas and fluids progressively heat and alter the SCLM, generating horizontal heterogeneity in both isotopic composition and seismic signatures (Hou et al., 2015a; Hou et al., 2015b).

The Eocene flare-up likely thickened the UDMB arc root by mafic underplating and addition of cumulates (Wan et al., 2018). Most Eocene magmatic rocks are enriched in F, S and H_2O and some have lamprophyric compositions with high contents of volatiles; both magma types are supposed to have originated from melting of refertilized SCLM (Salehi Nejad et al., 2020). Under reducing conditions, mafic cumulates can contain significant sulfide minerals (Lee et al., 2012), which could sink to the base of the crust and be metamorphosed into garnet-bearing gabbros ("arclogites"; Ducea et al., 2021), similar to the mechanism suggested for southeast Tibet (Hou et al., 2015a). Upwelling of asthenosphere following slab break-off during collision would provide enough heat to partially melt refractory sulfide-rich arclogites to generate mineralized adakitic rocks, a scenario that has been suggested for forming Cu deposits worldwide (Lee et al., 2012) and in the southeastern UDMB (Wan et al., 2018). Sulfide-bearing cumulates are refractory and thus might avoid being remelted during normal subduction (<1200 °C), but can be remelted under conditions of asthenospheric upwelling (>1400 °C) (Lee et al., 2012). Consequently, such upwelling might have promoted the genesis of giant Miocene porphyry deposits in southeast Tibet (Hou et al., 2015a) and in the southeastern UDMB. Remelting these cumulates can also release volatiles which could transport Cu complexes and other metals (Zajacz et al., 2012; Zajacz and Halter, 2009). Copper could mainly originate from decompression melting of Cu-bearing sulfides in the newly-formed lower mafic continental crust and/or from metal-rich lithospheric mantle (Hou et al., 2020). Further fractionation and AFC processing of sulfide-rich secondary melts can concentrate Cu ore-bearing melts and fluids. As previously noted, slab breakoff and asthenospheric upwelling (the heater) is consistent with geophysical data for the southeastern UDMB (Motaghi et al., 2015).

Another consideration for forming Cu deposits is crustal thickening associated with continental collision, which fosters garnet formation and fractionation, enriching the magma in Fe^{3+} (Lee and Tang, 2020). This can lead to the oxidation of residual magmas, releasing Cu from sulfides into magmatic fluids which can later concentrate Cu in the top of shallow plutons (Lee and Tang, 2020). This scenario can explain the close association of adakitic rocks and Cu—Au mineralization but does not explain the occurrence of similarly-aged barren and mineralized adakitic rocks in same areas of the southeastern UDMB. Additionally, the lack of an increase in SO_3 of apatite with decreasing age indicates that garnet plays a minor role in shaping the chemistry of Miocene magmas (Fig. 7F).

We therefore suggest that the lithospheric mantle beneath the southeastern UDMB has been refertilized in Cu during Late Cretaceous to Oligocene but mostly during the Middle-Late Eocene high magmatic

fluxes, and then was tapped by mantle melting triggered by asthenosphere upwelling. We also suggest that a refertilized, hot and volatile-rich lithospheric mantle could have significant control on porphyry Cu deposits in the southeastern UDMB, as suggested for southeast Tibet by studies on the magmatic rocks and ore deposits along with conventional bulk rock Nd and zircon Hf isotopes (Hou et al., 2015a; Hou et al., 2015b; Xu et al., 2021), empirical studies (Griffin et al., 2013; Griffin et al., 2009) as well as apatite trace elements and Sr isotopes (Xu et al., 2021) and Cu isotopes from both fertile and barren rocks (Zheng et al., 2018).

6.5. Arabia-Iran collision and magmatism

The principal objective of our study is to examine how convergent margin magmatism changes from subduction to collision. In the Himalaya-Tibet region there is a ~ 10 Myr gap in magmatism between subduction termination at 65–50 Ma and the proposed breakoff of the Neo-Tethyan oceanic slab at 55–50 Ma (Kapp et al., 2005; Ma et al., 2016; Wang et al., 2018). Kapp et al. (2005) argues that a magmatic flare-up was caused by the breakoff. Zircon Hf isotope data show that Himalayan-Tibet *syn*-collisional (<55 Ma) igneous rocks have more heterogeneous $\varepsilon Hf_{(t)}$ than pre-collisional subduction-related rocks, likely reflecting increased assimilation of thickened crust (Alexander et al., 2019).

All southeastern UDMB igneous rocks show subduction-related trace element signatures and temporal trends in magmatic, geochemical and isotopic patterns from Late Cretaceous to Pleistocene. These variations must reflect changes in the geometry and buoyancy of the subducting Neotethyan lithosphere and the responses of the overriding plate, first to slab rollback accompanied by extension in the Iranian Plateau during the Eocene, and then to the progression of Arabia-Iran collision beginning in Late Oligocene time accompanied by compression.

UDMB magmatism began with normal continental arc activity during the Late Cretaceous and then became quiescent in Paleocene and Early Eocene time. Early to Middle Paleocene magmatic quiescence may have been caused by a decreased dip of slab or a flat-slab subduction (e.g., Moghadam et al., 2020), which would be accompanied by compression in the overlying plate. Subduction of very young and buoyant oceanic lithosphere may have been responsible (e.g., Hu et al., 2016; Espurt et al., 2008), perhaps including subduction of the spreading ridge that once existed between Arabia and Iran.

The increase in the slab dip is an effective mechanism to cause the trench migration during Eocene (e.g., Hafkenscheid et al., 2006; Olbertz et al., 1997; Wortel and Spakman, 2000). This rollback may reflect the initial subduction of older and denser oceanic lithosphere that lay to the south of the subducted Neotethyan spreading axis. This slab began to roll back, exerting extensional stresses on overriding Iranian lithosphere, much the same as the present situation of the Aegean Sea and subducting African plate. This mechanism generated extension in the overlying Iranian crust which produced extensive magmatism across Iran, in both the magmatic front and back-arc. Extension within the Iranian plateau was associated with exhumation of core complexes such as the Saghand metamorphic complex (Fig. 1A), remelting continental crust and generating migmatites, granites and granodiorites with zircon U—Pb and mica $^{39}Ar/^{40}Ar$ ages of 47–42 Ma (Kargaranbafghi and Neubauer, 2015; Kargaranbafghi et al., 2015; Ramezani and Tucker, 2003). Extension was accompanied by subsidence of sedimentary basins, leaving thick sequences of deep-water limestones and/or tuffites and interlayered lavas within the Iranian Plateau. The Middle to Late Eocene magmatic flare-up within the Iranian plateau and granitization within the Saghand core complex are supposed to reflect the melting of crustal components (e.g., Kargaranbafghi and Neubauer, 2015; Verdel et al., 2011). However, this is not consistent with our recent isotopic data, at least for the magmatic flare-up, which show that mantle inputs with minor crustal contamination dominated during the Eocene flare-up.

Slab breakoff in Miocene time (<20 Ma) may also have occurred, since a well-defined subducted slab is not present beneath Iran west of the Makran today (Stern et al., 2021). However, the relationships between magma generation and their geochemical signatures during the transition between the initial Arabia-Iran collision and post-collisional period previously were unresolved in the UDMB of Iran. Our results are graphically summarized in Fig. 8 and show that there are geochemical-isotopic differences between subduction-related and collision-related magmatism and that these changes began when Arabia-Iran "soft" collision started at ~32 Ma. We suggest that both a metasomatized mantle (for Oligocene rocks with unradiogenic $\varepsilon Nd_{(t)}$, but moderately high $^{87}Sr/^{86}Sr_{(t)}$ compared to most Eocene and Miocene rocks) and a continental crust to foster assimilation continued to play important roles in magmatism after the onset of soft collision between Arabia and Iran in the Early Oligocene (at *ca* 32 Ma). The onset of collision is also marked by isotopic perturbation of bulk-rock $\varepsilon Nd_{(t)}$ and zircon $\varepsilon Hf_{(t)}$ and $\delta^{18}O$ values, indicating more assimilation of continental crust about the time that collision began. The increased heterogeneity of $\varepsilon Nd_{(t)}$, $\varepsilon Hf_{(t)}$ and $\delta^{18}O$ and greater degrees of assimilation probably reflect thickening of the continental crust after collision began at *ca* 32 Ma, which had a noticeable effect on magmatism. However, it should also be taken into consideration that the "soft" collision beginning ~32 Ma means that transitional crust of the Arabian passive margin and overlying sediments began to be subducted and these may be reflected in magmatic compositions. Furthermore, because this subducted lithosphere was more buoyant than oceanic lithosphere, it resisted subduction more, leading to more compression and thickening in the overriding plate. This increasingly disrupted the arc magma plumbing system, leading to increased interaction of mantle-derived magmas with the Iranian continental crust.

Post-collisional rocks (<20 Ma) have mostly mantle-like $\varepsilon Nd_{(t)}$, $\varepsilon Hf_{(t)}$ and $\delta^{18}O$ values that are more homogeneous than in ~Early Oligocene to Early Miocene (~32–20 Ma) rocks, although some younger, Middle Miocene samples have low bulk rock $\varepsilon Nd_{(t)}$ values (Fig. 6E). We also note that post-collisional rocks from SE Tibet show a decrease in $\varepsilon Hf_{(t)}$ after collision with India (from 55 Ma to 15 Ma) (Hou et al., 2015a; Hou et al., 2015b). This indicates that the magmas assimilated more crustal components during ascent through the thick and heterogeneous crust. However, although the crustal thickness continued to increase with decreasing age in the southeastern UDMB, most <20 Ma samples have high zircon $\varepsilon Hf_{(t)}$ values. These relationships could have several explanations: (1) This could suggest that melt conduits became better organized so that mantle-derived magmas interacted less with the continental crust through time, as suggested for similar Hf isotopic variations in magmatic rocks from the Alborz-Azerbaijan magmatic belt (Sepidbar et al., 2019); (2) Interaction of Miocene magmas with juvenile crust formed during the Eocene flare-up would not result in Hf-isotope perturbations; and (3) Miocene (<20 Ma) magmatic pulses injected into the magmatic lower crust could cannibalize previous intrusions with progressively less isotopic contrast due to dilution with mantle-derived magmas (Storck et al., 2020). High-temperature melting of lower-crust could also decompose zircons, releasing more Hf into the melts.

We also suggest that the breakoff of the Neo-Tethyan slab following collision promoted asthenospheric upwelling that contributed to melting subduction-modified subcontinental lithospheric mantle and lower crust "arclogites" to produce magmas with low $\varepsilon Nd_{(t)}$ and cause intense southeastern UDMB magmatism. These observations suggest that different magma-generation mechanisms dominated before, during, and after initial Arabia-Iran collision *ca* 32 Ma. Assuming convergence velocities of ~3 cm/yr. between Arabia and Iran during Neogene (Van de Zedde and Wortel, 2001), it is suggested that the subducting slab broke off ~10 m.yr. after collision began at 32 Ma (Hafkenscheid et al., 2006), which is consistent with the seismic tomography (e.g., Kaban et al., 2018), and the relative isotopic homogeneity in ~20 Ma magmatism (*this study*). Slab break-off was associated with Iranian plateau

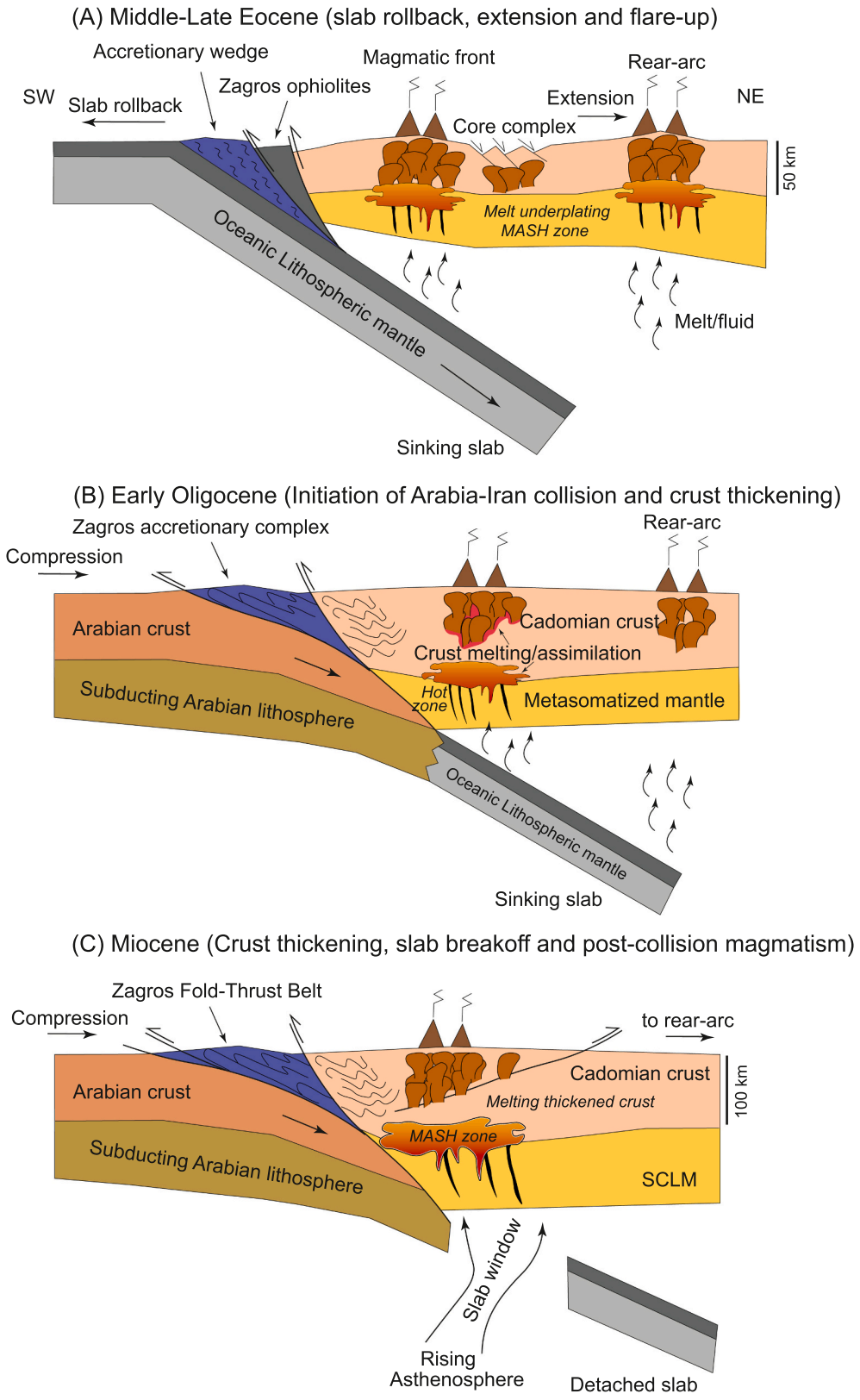

Fig. 8. Simplified cross-section showing different Middle-Late Eocene, Early Oligocene and Miocene magmatic episodes. Black dikes display melt conduits for primitive basaltic melts to enter the Melting- Assimilation- Storage and Homogenization (MASH) zones in deep lower crust. See text for further discussion.

uplift, the heating and consequent thinning of the lithosphere and then subsequent Iranian Plateau magmatism, which is geochemically different (mostly OIB-type lavas) than those involved in southeastern UDMB magmatism (Francois et al., 2014a; Francois et al., 2014b; Hafkenscheid et al., 2006).

7. Conclusions

The SE segment of the UDMB provides an outstanding opportunity to see how a magmatic arc evolves compositionally and isotopically from subduction through collision. Five stages can be identified: 1) normal continental-arc magmatism during the Late Cretaceous; 2) Arc quiescence in Paleocene and Early Eocene time; 3) Middle-Late Eocene extensional arc magmatism related to slab rollback; 4) Early collision and subduction of Arabian transitional crust and overlying sediments beginning in the Early Oligocene; and 5) Slab breakoff, asthenospheric upwelling, and associated adakitic magmatism in Middle Miocene and younger time. Northward subduction of the Neotethyan oceanic plate initiated UDMB magmatism, following an amagmatic period during the Paleocene-Early Eocene shortening episode and then strong extension during the Middle to Late Eocene to induce high-flux magmatism. Late Cretaceous and Eocene magmatic activity are isotopically variable; Eocene magmas are more geochemically variable due to the concomitant extension and flare-up at that time. Extension ended as Arabia approached, and magmatism changed fundamentally after collision with Arabia started at *ca* 32 Ma. The collision had a strong effect on magmatic compositions, yielding a thick continental crust with predominant adakitic magmatism and Cu mineralization.

Supplementary data to this article can be found online at https://doi.org/10.1016/j.earscirev.2022.103930.

Declaration of Competing Interest

None.

Acknowledgments

This study was funded by the "National Key Research and Development Program of China (2016YFE0203000)", "Chinese Academy of Sciences, President's International Fellowship Initiative (PIFI, 2019VCB0013)". Financial support was also received from the Alexander von Humboldt Foundation in the form of a senior research grant and GEOMAR Helmholtz Centre while preparing these results for publication. The analytical data were also obtained using instrumentation funded by ARC LIEF, DEST Systemic Infrastructure Grants, NCRIS/AuScope, industry partners and Macquarie University. This is contribution 1687 from the ARC Centre of Excellence for Core to Crust Fluid Systems (http://www.ccfs.mq.edu.au) and 1486 in the GEMOC Key Centre (http://www.gemoc.mq.edu.au). J.F.S. acklowledges financial support by FCT (Fundação para a Ciência e Tecnologia), through Geobiotec (UIDB/04035/2020) for Sr-Nd isotope analyses. This is UTD Geosciences contribution 1678. M.N.D. acknowledges support from the Romanian Executive Agency for Higher Education, Research, Development and Innovation Funding (UEFISCDI) project PN-III-P4-ID-PCCF-2016-0014. We are very grateful to three anonymous reviewers for their constructive reviews of the manuscript. Editorial suggestions by A. Gomez-Tuena and Y. Liu are also appreciated. All logistical support for the field work came from Damghan University, Iran. All data underlying the finding of this paper can be accessed from "Supplementary Tables".

References

Aghazadeh, M., Hou, Z.Q., Badrzadeh, Z., Zhou, L.M., 2015. Temporal-spatial distribution and tectonic setting of porphyry copper deposits in Iran: constraints from zircon U-Pb and molybdenite Re-Os geochronology. Ore Geol. Rev. 70, 385–406.

Alexander, E., Wielicki, M., Harrison, T., DePaolo, D., Zhao, Z., Zhu, D., 2019. Hf and Nd isotopic constraints on pre-and syn-collisional crustal thickness of southern Tibet. J. Geophys. Res. Solid Earth 124 (11), 11038–11054.

Allen, M.B., Armstrong, H.A., 2008. Arabia–Eurasia collision and the forcing of mid-Cenozoic global cooling. Palaeogeogr. Palaeoclimatol. Palaeoecol. 265 (1–2), 52–58.

Asadi, S., 2018. Triggers for the generation of post–collisional porphyry Cu systems in the Kerman magmatic copper belt, Iran: New constraints from elemental and isotopic (Sr–Nd–Hf–O) data. Gondwana Res. 64, 97–121.

Asadi, S., Moore, F., Zarasvandi, A., 2014. Discriminating productive and barren porphyry copper deposits in the southeastern part of the central Iranian volcano-plutonic belt, Kerman region, Iran: a review. Earth Sci. Rev. 138, 25–46.

Asiabanha, A., Foden, J., 2012. Post-collisional transition from an extensional volcano-sedimentary basin to a continental arc in the Alborz Ranges, N-Iran. Lithos 148, 98–111.

Atapour, H., Aftabi, A., 2021. Petrogeochemical evolution of calcalkaline, shoshonitic and adakitic magmatism associated with Kerman Cenozoic arc porphyry copper mineralization, southeastern Iran: a review. Lithos 106261.

Babazadeh, S., Ghorbani, M.R., Brocker, M., D'Antonio, M., Cottle, J., Gebbing, T., Mazzeo, F.C., Ahmadi, P., 2017. Late Oligocene-Miocene mantle upwelling and interaction inferred from mantle signatures in gabbroic to granitic rocks from the Urumieh-Dokhtar arc, south Ardestan, Iran. Int. Geol. Rev. 59 (12), 1590–1608.

Balica, C., Ducea, M., Gehrels, G., Kirk, J., Roban, R., Luffi, P., Chapman, J., Triantafyllou, A., Guo, J., Stoica, A., 2020. A zircon petrochronologic view on granitoids and continental evolution. Earth Planet. Sci. Lett. 531, 116005.

Ballato, P., Uba, C.E., Landgraf, A., Strecker, M.R., Sudo, M., Stockli, D.F., Friedrich, A., Tabatabaei, S.H., 2011. Arabia-Eurasia continental collision: Insights from late Tertiary foreland-basin evolution in the Alborz Mountains, northern Iran. Geol. Soc. Am. Bull. 123 (1–2), 106–131.

Ballato, P., Stockli, D.F., Ghassemi, M.R., Landgraf, A., Strecker, M.R., Hassanzadeh, J., Friedrich, A., Tabatabaei, S.H., 2013. Accommodation of transpressional strain in the Arabia-Eurasia collision zone: New constraints from (U-Th)/He thermochronology in the Alborz mountains, North Iran. Tectonics 32 (1), 1–18.

Barth, M.G., Foley, S.F., Horn, I., 2002. Partial melting in Archean subduction zones: constraints from experimentally determined trace element partition coefficients between eclogitic minerals and tonalitic melts under upper mantle conditions. Precambrian Res. 113 (3–4), 323–340.

Belousova, E., Griffin, W., O'Reilly, S.Y., Fisher, N., 2002a. Apatite as an indicator mineral for mineral exploration: trace-element compositions and their relationship to host rock type. J. Geochem. Explor. 76 (1), 45–69.

Belousova, E.A., Griffin, W.L., O'Reilly, S.Y., Fisher, N.I., 2002c. Igneous zircon: trace element composition as an indicator of source rock type. Contrib. Mineral. Petrol. 143 (5), 602–622.

Bindeman, I.N., Colón, D., Wotzlaw, J.-F., Stern, R., Chiaradia, M., Guillong, M., 2021. Young Silicic Magmatism of the Greater Caucasus, Russia, with implication for its delamination origin based on zircon petrochronology and thermomechanical modeling. J. Volcanol. Geotherm. Res. 412, 107173.

Boudreau, A., Kruger, F., 1990. Variation in the composition of apatite through the Merensky cyclic unit in the western Bushveld Complex. Econ. Geol. 85 (4), 737–745.

Cao, M.J., Li, G.M., Qin, K.Z., Seitmuratova, E.Y., Liu, Y.S., 2012. Major and trace element characteristics of apatites in granitoids from Central Kazakhstan: implications for petrogenesis and mineralization. Resour. Geol. 62 (1), 63–83.

Castro, A., Aghazadeh, M., Badrzadeh, Z., Chichorro, M., 2013. Late Eocene-Oligocene post-collisional monzonitic intrusions from the Alborz magmatic belt, NW Iran. An example of monzonite magma generation from a metasomatized mantle source. Lithos 180, 109–127.

Chaharlang, R., Ducea, M.N., Ghalamghash, J., 2020. Geochemical evidences for quantifying crustal thickness over time in the Urumieh-Dokhtar magmatic arc (Iran). Lithos 374–375.

Chapman, J.B., Ducea, M.N., DeCelles, P.G., Profeta, L., 2015. Tracking changes in crustal thickness during orogenic evolution with Sr/Y: an example from the north American Cordillera. Geology 43 (10), 919–922.

Chauvel, C., Blichert-Toft, J., 2001. A hafnium isotope and trace element perspective on melting of the depleted mantle. Earth Planet. Sci. Lett. 190 (3–4), 137–151.

Chiaradia, M., 2009. Adakite-like magmas from fractional crystallization and melting-assimilation of mafic lower crust (Eocene Macuchi arc, Western Cordillera, Ecuador). Chem. Geol. 265 (3–4), 468–487.

Chiu, H.Y., Chung, S.L., Zarrinkoub, M.H., Mohammadi, S.S., Khatib, M.M., Iizuka, Y., 2013. Zircon U-Pb age constraints from Iran on the magmatic evolution related to Neotethyan subduction and Zagros orogeny. Lithos 162, 70–87.

Chiu, H.Y., Chung, S.L., Zarrinkoub, M.H., Melkonyan, R., Pang, K.N., Lee, H.Y., Wang, K.L., Mohammadi, S.S., Khatib, M.M., 2017. Zircon Hf isotopic constraints on magmatic and tectonic evolution in Iran: Implications for crustal growth in the Tethyan orogenic belt. J. Asian Earth Sci. 145, 652–669.

DeCelles, P.G., Ducea, M.N., Kapp, P., Zandt, G., 2009. Cyclicity in Cordilleran orogenic systems. Nat. Geosci. 2 (4), 251–257.

Defant, M.J., Drummond, M.S., 1990. Derivation of some modern arc magmas by melting of young subducted lithosphere. Nature 347 (6294), 662–665.

Deng, C., Wan, B., Dong, L., Talebian, M., Windley, B.F., Dadashzadeh, H., Mohammadi, B., Barati, B., 2018. Miocene porphyry copper deposits in the Eastern Tethyan orogenic belt: using Sr, O isotopes and Sr/Y ratios to predict the source of ore-related and ore-barren magmas. Gondwana Res. 62, 14–26.

Duan, X.-X., Chen, B., Sun, K.-K., Wang, Z.-Q., Yan, X., Zhang, Z., 2019. Accessory mineral chemistry as a monitor of petrogenetic and metallogenetic processes: a comparative study of zircon and apatite from Wushan Cu- and Zhuxiling W(Mo)-mineralization-related granitoids. Ore Geol. Rev. 111.

Ducea, M.N., Paterson, S.R., DeCelles, P.G., 2015. High-volume magmatic events in subduction systems. Elements 11 (2), 99–104.

Ducea, M.N., Chapman, A.D., Bowman, E., Balica, C., 2020. Arclogites and their role in continental evolution; part 2: relationship to batholiths and volcanoes, density and foundering, remelting and long-term storage in the mantle. Earth Sci. Rev. 103476.

Ducea, M.N., Chapman, A.D., Bowman, E., Triantafyllou, A., 2021. Arclogites and their role in continental evolution; part 1: background, locations, petrography, geochemistry, chronology and thermobarometry. Earth Sci. Rev. 214, 103375.

Espurt, N., Funiciello, F., Martinod, J., Guillaume, B., Regard, V., Faccenna, C., Brusset, S., 2008. Flat subduction dynamics and deformation of the South American plate: insights from analog modeling. Tectonics 27 (3).
Farner, M.J., Lee, C.-T.A., 2017. Effects of crustal thickness on magmatic differentiation in subduction zone volcanism: a global study. Earth Planet. Sci. Lett. 470, 96–107.
Francois, T., Agard, P., Bernet, M., Meyer, B., Chung, S.L., Zarrinkoub, M.H., Buroy, E., Monie, P., 2014a. Cenozoic exhumation of the internal Zagros: first constraints from low-temperature thermochronology and implications for the build-up of the Iranian plateau. Lithos 206, 100–112.
Francois, T., Burov, E., Agard, P., Meyer, B., 2014b. Buildup of a dynamically supported orogenic plateau: numerical modeling of the Zagros/Central Iran case study. Geochem. Geophys. Geosyst. 15 (6), 2632–2654.
Griffin, W., O'Reilly, S.Y., Stabel, A., 1988. Mantle metasomatism beneath western Victoria, Australia: II. Isotopic geochemistry of Cr-diopside lherzolites and Al-augite pyroxenites. Geochim. Cosmochim. Acta 52 (2), 449–459.
Griffin, W.L., O'Reilly, S.Y., Afonso, J.C., Begg, G.C., 2009. The composition and evolution of lithospheric mantle: a re-evaluation and its tectonic implications. J. Petrol. 50 (7), 1185–1204.
Griffin, W.L., Begg, G.C., O'Reilly, S.Y., 2013. Continental-root control on the genesis of magmatic ore deposits. Nat. Geosci. 6 (11), 905–910.
Hafkenscheid, E., Wortel, M., Spakman, W., 2006. Subduction history of the Tethyan region derived from seismic tomography and tectonic reconstructions. J. Geophys. Res. Solid Earth 111 (B8).
Halter, W.E., Heinrich, C.A., Pettke, T., 2005. Magma evolution and the formation of porphyry Cu–au ore fluids: evidence from silicate and sulfide melt inclusions. Mineral. Deposita 39 (8), 845–863.
Hidalgo, P.J., Rooney, T.O., 2014. Petrogenesis of a voluminous Quaternary adakitic volcano: the case of Baru volcano. Contrib. Mineral. Petrol. 168 (3).
Hollings, P., Cooke, D., Clark, A., 2005. Regional geochemistry of tertiary igneous rocks in Central Chile: Implications for the geodynamic environment of giant porphyry copper and epithermal gold mineralization. Econ. Geol. 100 (5), 887–904.
Hosseini, M.R., Hassanzadeh, J., Alirezaei, S., Sun, W., Li, C.-Y., 2017. Age revision of the Neotethyan arc migration into the southeast Urumieh-Dokhtar belt of Iran: geochemistry and U–Pb zircon geochronology. Lithos. 284, 296–309.
Hou, Z.Q., Zhang, H.R., 2015. Geodynamics and metallogeny of the eastern Tethyan metallogenic domain. Ore Geol. Rev. 70, 346–384.
Hou, Z., Duan, L., Lu, Y., Zheng, Y., Zhu, D., Yang, Z., Yang, Z., Wang, B., Pei, Y., Zhao, Z., 2015a. Lithospheric architecture of the Lhasa terrane and its control on ore deposits in the Himalayan-Tibetan orogen. Econ. Geol. 110 (6), 1541–1575.
Hou, Z., Yang, Z., Lu, Y., Kemp, A., Zheng, Y., Li, Q., Tang, J., Yang, Z., Duan, L., 2015b. A genetic linkage between subduction- and collision-related porphyry Cu deposits in continental collision zones. Geology 43 (3), 247–250.
Hou, Z., Yang, Z., Wang, R., Zheng, Y., 2020. Further discussion on porphyry Cu-Mo-Au deposit formation in Chinese mainland. Earth Sci. Front. 27 (2), 20.
Hronsky, J.M., Groves, D.I., Loucks, R.R., Begg, G.C., 2012. A unified model for gold mineralisation in accretionary orogens and implications for regional-scale exploration targeting methods. Mineral. Deposita 47 (4), 339–358.
Hu, J., Liu, L., Hermosillo, A., Zhou, Q., 2016. Simulation of late Cenozoic South American flat-slab subduction using geodynamic models with data assimilation. Earth Planet. Sci. Lett. 438, 1–13.
Hu, F., Wu, F., Chapman, J.B., Ducea, M.N., Ji, W., Liu, S., 2020. Quantitatively tracking the elevation of the Tibetan Plateau since the cretaceous: Insights from whole-rock Sr/Y and La/Yb ratios. Geophys. Res. Lett. 47 (15) e2020GL089202.
Iveson, A.A., Rowe, M.C., Webster, J.D., Neill, O.K., 2018. Amphibole-, clinopyroxene- and plagioclase-melt partitioning of trace and economic metals in halogen-bearing rhyodacitic melts. J. Petrol. 59 (8), 1579–1604.
Jamali, H., Dilek, Y., Daliran, F., Yaghubpur, A., Mehrabi, B., 2010. Metallogeny and tectonic evolution of the Cenozoic Ahar-Arasbaran volcanic belt, northern Iran. Int. Geol. Rev. 52 (4–6), 608–630.
Kaban, M.K., Petrunin, A.G., El Khrepy, S., Al-Arifi, N., 2018. Diverse continental subduction scenarios along the Arabia-Eurasia collision zone. Geophys. Res. Lett. 45 (14), 6898–6906.
Kapp, P., Yin, A., Harrison, T.M., Ding, L., 2005. Cretaceous-Tertiary shortening, basin development, and volcanism in Central Tibet. Geol. Soc. Am. Bull. 117 (7–8), 865–878.
Kargaranbafghi, F., Neubauer, F., 2015. Lithospheric thinning associated with formation of a metamorphic core complex and subsequent formation of the Iranian plateau. GSA Today 25 (7), 4–8.
Kargaranbafghi, F., Neubauer, F., Genser, J., 2015. Rapid Eocene extension in the Chapedony metamorphic core complex, Central Iran: constraints from Ar-40/Ar-39 dating. J. Asian Earth Sci. 106, 156–168.
Kheirkhah, M., Neill, I., Allen, M.B., Emami, M.H., Ghadimi, A.S., 2020. Distinct sources for high-K and adakitic magmatism in SE Iran. J. Asian Earth Sci. 196, 104355.
Lee, C.T.A., Tang, M., 2020. How to make porphyry copper deposits. Earth Planet. Sci. Lett. 529.
Lee, C.-T.A., Luffi, P., Chin, E.J., Bouchet, R., Dasgupta, R., Morton, D.M., Le Roux, V., Yin, Q.-Z., Jin, D., 2012. Copper systematics in arc magmas and implications for crust-mantle differentiation. Science 336 (6077), 64–68.
Li, H., Hermann, J., 2017. The effect of fluorine and chlorine on trace element partitioning between apatite and sediment melt at subduction zone conditions. Chem. Geol. 473, 55–73.
Lieu, W.K., Stern, R.J., 2019. The robustness of Sr/Y and La/Yb as proxies for crust thickness in modern arcs. Geosphere 15 (3), 621–641.
Liu, A.-L., Wang, Q., Zhu, D.-C., Zhao, Z.-D., Liu, S.-A., Wang, R., Dai, J.-G., Zheng, Y.-C., Zhang, L.-L., 2018. Origin of the ca. 50 Ma Linzizong shoshonitic volcanic rocks in the eastern Gangdese arc, southern Tibet. Lithos 304, 374–387.
Lu, Y., Loucks, R., Fiorentini, M., McCuaig, T., Evans, N.J., Yang, Z.-M., Hou, Z.-Q., Kirkland, C.L., Avila, L.P., Kobussen, A., 2016. Zircon compositions as a pathfinder for porphyry Cu±Mo±Au deposits. Soc. Econ. Geol. Special Pub. Series 19, 329–347.
Ma, X., Xu, Z., Meert, J.G., 2016. Eocene slab breakoff of Neotethys as suggested by dioritic dykes in the Gangdese magmatic belt, southern Tibet. Lithos 248, 55–65.
Madanipour, S., Ehlers, T.A., Yassaghi, A., Rezaeian, M., Enkelmann, E., Bahroudi, A., 2013. Synchronous deformation on orogenic plateau margins: Insights from the Arabia–Eurasia collision. Tectonophysics 608, 440–451.
Madanipour, S., Ehlers, T.A., Yassaghi, A., Enkelmann, E., 2017. Accelerated middle Miocene exhumation of the Talesh Mountains constrained by U-Th/He thermochronometry: evidence for the Arabia-Eurasia collision in the NW Iranian Plateau. Tectonics 36 (8), 1538–1561.
Matenco, L., Krezsek, C., Merten, S., Schmid, S., Cloetingh, S., Andriessen, P., 2010. Characteristics of collisional orogens with low topographic build-up: an example from the Carpathians. Terra Nova 22 (3), 155–165.
McQuarrie, N., van Hinsbergen, D.J.J., 2013. Retrodeforming the Arabia-Eurasia collision zone: Age of collision versus magnitude of continental subduction. Geology 41 (3), 315–318.
Meurer, W., Boudreau, A.E., 1996. An evaluation of models of apatite compositional variability using apatite from the Middle Banded series of the Stillwater Complex, Montana. Contrib. Mineral. Petrol. 125 (2–3), 225–236.
Moghadam, M.C., Tahmasbi, Z., Ahmadi-Khalaji, A., Santos, J.F., 2018. Petrogenesis of Rabor-Lalehzar magmatic rocks (SE Iran): Constraints from whole rock chemistry and Sr-Nd isotopes. Chemie Der Erde-Geochem. 78 (1), 58–77.
Moghadam, H.S., Li, Q.L., Li, X.H., Stern, R.J., Levresse, G., Santos, J.F., Lopez Martinez, M., Ducea, M.N., Ghorbani, G., Hassannezhad, A., 2020. Neotethyan subduction ignited the iran arc and backarc differently. J. Geophys. Res. Solid Earth 125 (5).
Moghadam, H.S., Li, Q., Griffin, W., Stern, R., Santos, J., Lucci, F., Beyarslan, M., Ghorbani, G., Ravankhah, A., Tilhac, R., 2021. Prolonged magmatism and growth of the Iran-Anatolia Cadomian continental arc segment in Northern Gondwana. Lithos 384-385, 105940.
Moritz, R., Rezeau, H., Ovtcharova, M., Tayan, R., Melkonyan, R., Hovakimyan, S., Ramazanov, V., Selby, D., Ulianov, A., Chiaradia, M., 2016. Long-lived, stationary magmatism and pulsed porphyry systems during Tethyan subduction to post-collision evolution in the southernmost Lesser Caucasus, Armenia and Nakhitchevan. Gondwana Res. 37, 465–503.
Motaghi, K., Tatar, M., Priestley, K., Romanelli, F., Doglioni, C., Panza, G.F., 2015. The deep structure of the Iranian Plateau. Gondwana Res. 28 (1), 407–418.
Mouthereau, F., Lacombe, O., Verges, J., 2012. Building the Zagros collisional orogen: timing, strain distribution and the dynamics of Arabia/Eurasia plate convergence. Tectonophysics 532, 27–60.
Nabelek, P.I., 2020. Petrogenesis of leucogranites in collisional orogens. Geol. Soc. Lond., Spec. Publ. 491 (1), 179–207.
Olbertz, D., Wortel, M., Hansen, U., 1997. Trench migration and subduction zone geometry. Geophys. Res. Lett. 24 (3), 221–224.
Omrani, J., Agard, P., Whitechurch, H., Benoit, M., Prouteau, G., Jolivet, L., 2008. Arc-magmatism and subduction history beneath the Zagros Mountains, Iran: a new report of adakites and geodynamic consequences. Lithos 106 (3–4), 380–398.
O'Reilly, S.Y., Griffin, W., 2013. Mantle Metasomatism, Metasomatism and the Chemical Transformation of Rock. Springer, pp. 471–533.
Palma, G., Barra, F., Reich, M., Valencia, V., Simon, A.C., Vervoort, J., Leisen, M., Romero, R., 2019. Halogens, trace element concentrations, and Sr-Nd isotopes in apatite from iron oxide-apatite (IOA) deposits in the Chilean iron belt: evidence for magmatic and hydrothermal stages of mineralization. Geochim. Cosmochim. Acta 246, 515–540.
Pan, L.-C., Hu, R.-Z., Bi, X.-W., Wang, Y., Yan, J., 2020. Evaluating magmatic fertility of Paleo-Tethyan granitoids in eastern Tibet using apatite chemical composition and Nd isotope. Ore Geol. Rev. 127.
Pang, K.-N., Chung, S.-L., Zarrinkoub, M.H., Mohammadi, S.S., Yang, H.-M., Chu, C.-H., Lee, H.-Y., Lo, C.-H., 2012. Age, geochemical characteristics and petrogenesis of Late Cenozoic intraplate alkali basalts in the Lut–Sistan region, eastern Iran. Chem. Geol. 306, 40–53.
Pang, K.-N., Chung, S.-L., Zarrinkoub, M.H., Li, X.-H., Lee, H.-Y., Lin, T.-H., Chiu, H.-Y., 2016. New age and geochemical constraints on the origin of Quaternary adakite-like lavas in the Arabia–Eurasia collision zone. Lithos 264, 348–359.
Profeta, L., Ducea, M.N., Chapman, J.B., Paterson, S.R., Gonzales, S.M.H., Kirsch, M., Petrescu, L., DeCelles, P.G., 2015. Quantifying crustal thickness over time in magmatic arcs. Sci. Rep. 5.
Prowatke, S., Klemme, S., 2006. Trace element partitioning between apatite and silicate melts. Geochim. Cosmochim. Acta 70 (17), 4513–4527.
Raeisi, D., Zhao, M., Babazadeh, S., Long, L.E., Hajsadeghi, S., Modabberi, S., 2021. Synthesis on productive, sub-productive and barren intrusions in the Urumieh-Dokhtar magmatic arc, Iran, constraints on geochronology and geochemistry. Ore Geol. Rev. 103997.
Ramezani, J., Tucker, R.D., 2003. The Saghand Region, Central Iran: U-Pb geochronology, petrogenesis and implications for Gondwana Tectonics. Am. J. Sci. 303 (7), 622–665.
Richards, J.P., 2009. Postsubduction porphyry Cu-Au and epithermal Au deposits: Products of remelting of subduction-modified lithosphere. Geology 37 (3), 247–250.
Richards, J.P., 2015. The oxidation state, and sulfur and Cu contents of arc magmas: implications for metallogeny. Lithos 233, 27–45.
Salehi Nejad, H., Ahmadipour, H., Moinzadeh, H., Moradian, A., Santos, J.F., 2020. Geochemistry and petrogenesis of Raviz-Shanabad intrusions (Southeastern UDMB): an evidence for Late Eocene magmatism. Int. Geol. Rev. 1–18.

Schisa, P., Boudreau, A., Djon, L., Tchalikian, A., Corkery, J., 2015. The Lac Des Iles palladium deposit, Ontario, Canada. Part II. Halogen variations in apatite. Mineral. Deposita 50 (3), 339–355.
Seghedi, I., Downes, H., 2011. Geochemistry and tectonic development of Cenozoic magmatism in the Carpathian–Pannonian region. Gondwana Res. 20 (4), 655–672.
Sepidbar, F., Shafaii Moghadam, H., Zhang, L., Li, J.-W., Ma, J., Stern, R.J., Lin, C., 2019. Across-arc geochemical variations in the Paleogene magmatic belt of Iran. Lithos 344-345, 280–296.
Sha, L.K., Chappell, B.W., 1999. Apatite chemical composition, determined by electron microprobe and laser-ablation inductively coupled plasma mass spectrometry, as a probe into granite petrogenesis. Geochim. Cosmochim. Acta 63 (22), 3861–3881.
Shafiei, B., Haschke, M., Shahabpour, J., 2009. Recycling of orogenic arc crust triggers porphyry Cu mineralization in Kerman Cenozoic arc rocks, southeastern Iran. Mineral. Deposita 44 (3), 265.
Siani, M.G., Lentz, D.R., Nazarian, M., 2020. Geochemistry of igneous rocks associated with mineral deposits in the Tarom-Hashtjin metallogenic province, NW Iran: an analysis of the controls on epithermal and related porphyry-style mineralization. Ore Geol. Rev. 103753.
Stern, C.R., Funk, J.A., Skewes, M.A., Arévalo, A., 2007. Magmatic anhydrite in plutonic rocks at the El Teniente Cu-Mo deposit, Chile, and the role of sulfur-and copper-rich magmas in its formation. Econ. Geol. 102 (7), 1335–1344.
Stern, C.R., Skewes, M.A., Arevalo, A., 2011. Magmatic evolution of the Giant El Teniente Cu-Mo Deposit, Central Chile. J. Petrol. 52 (7–8), 1591–1617.
Stern, R.J., Moghadam, H.S., Pirouz, M., Mooney, W., 2021. The geodynamic evolution of Iran. Annu. Rev. Earth Planet. Sci. 49, 9–36.
Storck, J.-C., Wotzlaw, J.-F., Karakas, Ö., Brack, P., Gerdes, A., Ulmer, P., 2020. Hafnium isotopic record of mantle-crust interaction in an evolving continental magmatic system. Earth Planet. Sci. Lett. 535, 116100.
Sun, S.-S., McDonough, W.-S., 1989. Chemical and isotopic systematics of oceanic basalts: implications for mantle composition and processes. Geol. Soc. Lond., Spec. Publ. 42 (1), 313–345.
Tadayon, M., Rossetti, F., Zattin, M., Nozaem, R., Calzolari, G., Madanipour, S., Salvini, F., 2017. The post-eocene evolution of the Doruneh Fault Region (Central Iran): the intraplate response to the reorganization of the Arabia-Eurasia Collision Zone. Tectonics 36, 3038–3064.
Tang, M., Ji, W.Q., Chu, X., Wu, A.B., Chen, C., 2020a. Reconstructing crustal thickness evolution from europium anomalies in detrital zircons. Geology 49 (1), 76–80.
Tang, M., Lee, C.-T.A., Ji, W.-Q., Wang, R., Costin, G., 2020b. Crustal thickening and endogenic oxidation of magmatic sulfur. Sci. Adv. 6 (31), eaba6342.
Tang, M., Chu, X., Hao, J., Shen, B., 2021. Orogenic quiescence in Earth's middle age. Science 371, 728–731.
Valley, J.W., Kinny, P.D., Schulze, D.J., Spicuzza, M.J., 1998. Zircon megacrysts from kimberlite: oxygen isotope variability among mantle melts. Contrib. Mineral. Petrol. 133 (1–2), 1–11.
Van de Zedde, D., Wortel, M., 2001. Shallow slab detachment as a transient source of heat at midlithospheric depths. Tectonics 20 (6), 868–882.
van der Boon, A., Kuiper, K.F., van der Ploeg, R., Cramwinckel, M.J., Honarmand, M., Sluijs, A., Krijgsman, W., 2021. Exploring a link between the Middle Eocene Climatic Optimum and Neotethys continental arc flare-up. Clim. Past 17 (1), 229–239.
Verdel, C., Wernicke, B.P., Hassanzadeh, J., Guest, B., 2011. A Paleogene extensional arc flare-up in Iran. Tectonics 30.
Wan, B., Deng, C., Najafi, A., Hezareh, M.R., Talebian, M., Dong, L., Chen, L., Xiao, W., 2018. Fertilizing porphyry Cu deposits through deep crustal hot zone melting. Gondwana Res. 60, 179–185.
Wang, R., Richards, J.P., Hou, Z.Q., Yang, Z.M., Gou, Z.B., DuFrane, S.A., 2014. Increasing magmatic oxidation state from paleocene to miocene in the eastern Gangdese Belt, Tibet: implication for collision-related porphyry Cu-Mo±Au mineralization. Econ. Geol. 109, 1943–1965.
Wang, R., Weinberg, R.F., Collins, W.J., Richards, J.P., Zhu, D.C., 2018. Origin of postcollisional magmas and formation of porphyry Cu deposits in southern Tibet. Earth Sci. Rev. 181, 122–143.
Watson, E.B., Green, T.H., 1981. Apatite/liquid partition coefficients for the rare earth elements and strontium. Earth Planet. Sci. Lett. 56, 405–421.
Williams, T.J., Candela, P.A., Piccoli, P.M., 1995. The partitioning of copper between silicate melts and two-phase aqueous fluids: an experimental investigation at 1 kbar, 800 C and 0.5 kbar, 850 C. Contrib. Mineral. Petrol. 121 (4), 388–399.
Wortel, M., Spakman, W., 2000. Subduction and slab detachment in the Mediterranean-Carpathian region. Science 290 (5498), 1910–1917.
Xu, B., Griffin, W.L., Hou, Z.-Q., Lu, Y., Belousova, E., Xu, J.-F., O'Reilly, S.Y., 2021. Recycled volatiles determine fertility of porphyry deposits in collisional settings. Am. Mineral. 106 (4), 656–661.
Xu, B., Hou, Z.-Q., Griffin, W.L., Zheng, Y.-C., Wang, T., Guo, Z., Hou, J., Santosh, M., O'Reilly, S.Y., 2021. Cenozoic lithospheric architecture and metallogenesis in Southeastern Tibet. Earth Sci. Rev. 214.
Yang, J.-H., Kang, L.-F., Peng, J.-T., Zhong, H., Gao, J.-F., Liu, L., 2018. In-situ elemental and isotopic compositions of apatite and zircon from the Shuikoushan and Xihuashan granitic plutons: Implication for Jurassic granitoid-related Cu-Pb-Zn and W mineralization in the Nanling Range, South China. Ore Geol. Rev. 93, 382–403.
Yeganehfar, H., Ghorbani, M.R., Shinjo, R., Ghaderi, M., 2013. Magmatic and geodynamic evolution of Urumieh-Dokhtar basic volcanism, Central Iran: major, trace element, isotopic, and geochronologic implications. Int. Geol. Rev. 55 (6), 767–786.
Zajacz, Z., Halter, W., 2009. Copper transport by high temperature, sulfur-rich magmatic vapor: evidence from silicate melt and vapor inclusions in a basaltic andesite from the Villarrica volcano (Chile). Earth Planet. Sci. Lett. 282 (1–4), 115–121.
Zajacz, Z., Candela, P.A., Piccoli, P.M., Walle, M., Sanchez-Valle, C., 2012. Gold and copper in volatile saturated mafic to intermediate magmas: Solubilities, partitioning, and implications for ore deposit formation. Geochim. Cosmochim. Acta 91, 140–159.
Zhang, Q., Willems, H., Ding, L., Gräfe, K.-U., Appel, E., 2012. Initial India-Asia continental collision and foreland basin evolution in the Tethyan Himalaya of Tibet: evidence from stratigraphy and paleontology. J. Geol. 120 (2), 175–189.
Zheng, Y.-C., Liu, S.-A., Wu, C.-D., Griffin, W.L., Li, Z.-Q., Xu, B., Yang, Z.-M., Hou, Z.-Q., O'Reilly, S.Y., 2018. Cu isotopes reveal initial Cu enrichment in sources of giant porphyry deposits in a collisional setting. Geology 47 (2), 135–138.